A&A 662, A33 (2022)
https://doi.org/10.1051/0004-6361/202039346

Astronomy & Astrophysics

The VIMOS Ultra Deep Survey: The reversal of the star-formation rate – density relation at $2 < z < 5$

B. C. Lemaux[1,2,3], O. Cucciati[4], O. Le Fèvre[1,⋆], G. Zamorani[4], L. M. Lubin[2], N. Hathi[5], O. Ilbert[1], D. Pelliccia[2,6], R. Amorín[7,8], S. Bardelli[4], P. Cassata[9,10], R. R. Gal[11], B. Garilli[12], L. Guaita[13,14], M. Giavalisco[15], D. Hung[11], A. Koekemoer[5], D. Maccagni[12], L. Pentericci[12], B. Ribeiro[16], D. Schaerer[17], E. Shah[2,⋆⋆], L. Shen[2,18,19], P. Staab[2], M. Talia[4], R. Thomas[20], A. R. Tomczak[2], L. Tresse[1], E. Vanzella[4], D. Vergani[4], and E. Zucca[4]

(Affiliations can be found after the references)

Received 5 September 2020 / Accepted 28 February 2022

ABSTRACT

Utilizing spectroscopic observations taken for the VIMOS Ultra-Deep Survey (VUDS), new observations from Keck/DEIMOS, and publicly available observations of large samples of star-forming galaxies, we report here on the relationship between the star-formation rate (SFR) and the local environment ($\delta_{\rm gal}$) of galaxies in the early universe ($2 < z < 5$). Unlike what is observed at lower redshifts ($z \lesssim 2$), we observe a definite, nearly monotonic increase in the average SFR with increasing galaxy overdensity over more than an order of magnitude in $\delta_{\rm gal}$. The robustness of this trend is quantified by accounting for both uncertainties in our measurements and galaxy populations that are either underrepresented or not present in our sample (e.g., extremely dusty star-forming and quiescent galaxies), and we find that the trend remains significant under all circumstances. This trend appears to be primarily driven by the fractional increase of galaxies in high-density environments that are more massive in their stellar content and are forming stars at a higher rate than their less massive counterparts. We find that, even after stellar mass effects are accounted for, there remains a weak but significant SFR–$\delta_{\rm gal}$ trend in our sample implying that additional environmentally related processes are helping to drive this trend. We also find clear evidence that the average SFR of galaxies in the densest environments increases with increasing redshift. These results lend themselves to a picture in which massive gas-rich galaxies coalesce into proto-cluster environments at $z \gtrsim 3$, interact with other galaxies or with a forming large-scale medium, subsequently using or losing most of their gas in the process, and begin to seed the nascent red sequence that is present in clusters at slightly lower redshifts.

Key words. galaxies: evolution – galaxies: high-redshift – galaxies: clusters: general – techniques: photometric – techniques: spectroscopic

1. Introduction

It has now been firmly established that dense environments at low to intermediate redshifts ($z \lesssim 1.5$) are generally hostile to star-formation activity. While the mechanisms underlying the establishment of such trends are still debated, observations have clearly shown that galaxies that inhabit low- to intermediate-redshift clusters are generally redder (e.g., Hansen et al. 2009; Peng et al. 2010; Cooper et al. 2010; Lemaux et al. 2012, 2019; Kovač et al. 2014; Balogh et al. 2016; Nantais et al. 2016, 2017; Cucciati et al. 2017; van der Burg et al. 2020), are less star-forming (e.g., Gómez et al. 2003; von der Linden et al. 2010; Muzzin et al. 2012; Tomczak et al. 2019; Old et al. 2020), and are more likely to have undergone recent quenching events (e.g., Tran et al. 2003; Wu et al. 2014; Lemaux et al. 2017; Socolovsky et al. 2018; Owers et al. 2019; Paccagnella et al. 2019) than coeval field samples. As a result, the general relationship between the average star-formation rate (SFR) of galaxies and galaxy density ($\delta_{\rm gal}$) up to $z \sim 1.5$ appears to be one of an anticorrelation. Furthermore, the presence of massive, red galaxies appears to persist in some overdense environments at least to $z \sim 2$ (e.g., Kodama et al. 2007; Strazzullo et al. 2013; Diener et al. 2015), However, there are hints that this relationship between SFR and $\delta_{\rm gal}$ observed at lower redshifts begins to break down or even reverse by $z \sim 1$–2. At these redshifts, several case studies from individual structures or relatively small field surveys have shown intriguing indications of this reversal, with galaxies that inhabit denser environments showing increased star formation activity relative to counterparts in more rarefied environments (e.g., Cucciati et al. 2006; Elbaz et al. 2007; Tran et al. 2010; Santos et al. 2014, 2015, though see also the discussion in Cooper et al. 2007 regarding the results presented in Cucciati et al. 2006). In a larger sample of ∼16 000 galaxies spanning 2.8 square degrees taken from the Deep Extragalactic Evolutionary Probe 2 (DEEP2; Davis et al. 2003; Newman et al. 2013), Cooper et al. (2008) found a clear reversal of the relationship between SFR and $\delta_{\rm gal}$ at $z \sim 1$ relative to that observed in the local universe. Galaxies that inhabit the most extreme environments (i.e., high-mass groups and clusters of galaxies) were, however, largely absent from the sample presented in Cooper et al. (2008). Recent results from Tomczak et al. (2019), in an analysis of ∼10 000 galaxies taken from the Observations of Redshift Evolution in Large Scale Environment (ORELSE; Lubin et al. 2009) survey that spanned field, group, and cluster environments at $z \sim 1$, found no such positive correlation between SFR and $\delta_{\rm gal}$ in aggregate. At slightly higher redshifts ($z \sim 1.2$), Old et al. (2020) also found a flat or negative trend between SFR and $\delta_{\rm gal}$ from ∼1500 cluster and field galaxies drawn from the Gemini Observations of Galaxies in Rich Early ENvironments (GOGREEN; Balogh et al. 2017, 2021) survey, with a stronger anticorrelation seen in the lower redshift portion of their sample ($z \sim 1$). Such seemingly conflicting results speak to the complex relationship between the SFR of galaxies and their environment

⋆ Deceased.
⋆⋆ LSSTC DSFP Fellow.

at intermediate redshift, which appears to vary considerably depending on the range of environments probed and across different structures. Clearly, however, this relationship has evolved dramatically by $z \sim 1$ relative to the local relation, and indications of a reversal at intermediate redshift are consistent with the early formation epochs inferred for massive galaxies in intermediate-redshift clusters (Hilton et al. 2009; Rettura et al. 2010; Raichoor et al. 2011; Lemaux et al. 2012; Fumagalli et al. 2016), as well as with the mere presence of massive and evolved galaxies at $z \sim 5$ (e.g., Mawatari et al. 2016; Lemaux et al. 2018). These lines of evidence strongly indicate that the peak of star-formation activity for massive cluster galaxies broadly lies at early epochs ($z > 2$).

This observational picture is corroborated by results from simulations in which it is estimated that forming clusters (i.e., proto-clusters) form the vast majority of their stellar content at early times, ~50% during the 1.5 Gyr period from $2 < z < 4$ (Chiang et al. 2017). During these epochs, it is predicted that proto-cluster environments become an important contribution to the overall comoving cosmic SFR density (SFRD), which is seen to peak at these redshifts (Madau & Dickinson 2014). While proto-clusters fill only ~3% of the comoving volume of the universe at these epochs, they are estimated to contribute 20–30% to the overall SFRD (Chiang et al. 2017; Muldrew et al. 2018), implying a rate of stellar mass assembly far outpacing that of the field. Concurrent to the peak in the cosmic SFRD, the rate of galaxies undergoing major mergers also appears to increase to these redshifts (e.g., López-Sanjuan et al. 2013; Tasca et al. 2014), suggesting that the seeds of the most massive cluster galaxies observed today are sewn both through in situ star formation and ex situ through galaxy merging in the extended proto-cluster environment.

While this picture is extremely exciting, definitive observational evidence at these redshifts has been lagging. Many searches for proto-clusters at such redshifts have been attempted. However, such searches are extremely challenging due to the extreme faintness of the galaxy populations. While photometric redshifts can be used to identify proto-cluster candidates in blank fields (e.g., Diener et al. 2013; Chiang et al. 2014) or around radio quasars (e.g., Hatch et al. 2014), without spectroscopic confirmation the authenticity of these candidates is suspect. Spectroscopic searches for proto-clusters are typically targeted at Lyman-alpha emitters (LAEs; Toshikawa et al. 2014, 2016, 2018, 2020; Dey et al. 2016) or Submillimeter galaxies (SMGs; Casey et al. 2015; Smolčić et al. 2017a; Greenslade et al. 2018; Lewis et al. 2018; Oteo et al. 2018; Cheng et al. 2020; Long et al. 2020), galaxies that can be either subdominant or extremely biased relative to the overall galaxy population (e.g., Cassata et al. 2015; Miller et al. 2015) and may trace overdensities differently than more typical populations (e.g., Shi et al. 2019; Guaita et al. 2020). The inhomogeneity inherent in this selection, combined with a lack of large, comparable field samples, makes any study of environmentally driven evolution difficult to interpret.

Still, there exist exciting case studies of high-redshift proto-cluster systems detected through these search techniques, where star-formation activity among member galaxies is seen to far outpace that of the coeval field (e.g., Greenslade et al. 2018; Miller et al. 2018; Shimakawa et al. 2018a; Noirot et al. 2018; Cheng et al. 2019, 2020; Hill et al. 2020). Several case studies probing more typical galaxies in proto-cluster environments at $z > 2$ also show similar behavior (e.g., Wang et al. 2016; Shimakawa et al. 2018a; Shi et al. 2020). Additionally, analysis of the ultraviolet luminosity function of photometrically selected proto-cluster candidate galaxies suggests that such behavior might be a general property of proto-cluster galaxies at high redshift (Ito et al. 2020). However, in order to confirm that this trend is indeed general in the high-redshift universe, rather than limited to a small number of proto-clusters or proto-clusters in a rare phase of their evolution, a spectroscopic census of a representative galaxy population in a large ensemble of forming overdensities in the early universe, as well as a comparably selected field sample, is required.

In this paper we present an investigation of the relationship between the SFR and galaxy density of a large sample of spectroscopically confirmed galaxies in the early universe ($2 \leq z \leq 5$). This sample is primarily drawn from observations taken with VIsible Multi-Object Spectrograph (VIMOS, Le Fèvre et al. 2003) as part of the VIMOS Ultra-Deep Survey (VUDS, Le Fèvre et al. 2015) across three well-studied extragalactic fields. Additional spectroscopic data were drawn from the VIMOS VLT Deep Survey (VVDS; Le Fèvre et al. 2013), the zCOSMOS survey (Lilly et al. 2007, 2009, Lilly et al., in prep.), a variety of other smaller public surveys, and new observations from the Keck DEep Imaging Multi-Object Spectrograph (DEIMOS, Faber et al. 2003) to create a sample of 6730 spectroscopically confirmed star-forming galaxies extending over a footprint of ~3 deg^2. These spectral observations were complemented by deep multiband imaging observations, which were used both for the estimate of high-quality photometric redshifts and an estimate of the instantaneous SFRs of galaxies. A weighted combination of spectroscopic and photometric information was used to create high-fidelity galaxy density maps with which to investigate the effect of environment on star formation activity at these redshifts.

The structure of the paper is as follows. In Sect. 2 we discuss the imaging and spectroscopic observations used for this study, the methods for estimating photometric redshifts, SFRs, and environment, as well as the representativeness of our spectral sample. In Sect. 3 we investigate the general relationship between SFR–$\delta_{\rm gal}$ and stellar mass–$\delta_{\rm gal}$ for our final sample, including the behavior of SFR–$\delta_{\rm gal}$ as a function of stellar mass and of redshift, and explore scenarios that may give rise to the observed trends. In Sect. 4 we summarize our results and present our main conclusions. Throughout this paper all magnitudes, including those in the infrared, are presented in the AB system (Oke & Gunn 1983; Fukugita et al. 1996) and distances are given in proper rather than comoving units. We adopt a concordance ΛCDM cosmology with $H_0 = 70\,{\rm km\,s^{-1}\,Mpc^{-1}}$, $\Omega_\Lambda = 0.73$, and $\Omega_{\rm M} = 0.27$. While abbreviated for convenience, throughout the paper stellar masses are presented in units of $h_{70}^{-2}\,M_*$, star formation rates in units of $h_{70}^{-2}\,M_*\,{\rm yr^{-1}}$, proper distances in units of h_{70}^{-1} kpc or Mpc, where $h_{70} \equiv H_0/70\,{\rm km^{-1}\,s\,Mpc}$.

2. Observations and spectral energy distribution fitting

The primary observations used for this study are drawn from VUDS (Le Fèvre et al. 2015), a massive 640-h (~80 night) spectroscopic campaign reaching extreme depths ($i' \lesssim 25$) over three well-studied extragalactic fields: the Cosmic Evolution Survey (COSMOS, Scoville et al. 2007) field, the Extended *Chandra* Deep Field South (ECDFS, Lehmer et al. 2005), and the first field of the Canada-France-Hawai'i Telescope Legacy Survey (CFHTLS-D1[1]) also known as the VVDS-02h field. These

[1] http://www.cfht.hawaii.edu/Science/CFHTLS/

observations are supplemented by a variety of publicly available imaging and spectroscopic data sets taken in the same three fields as well as our own follow-up observations. We describe the basic properties of these data below.

2.1. Imaging data and photometry

The imaging data relevant to this study have been discussed in detail in other papers and, as such, are only briefly described here. These data broadly include extremely deep ($m_{\rm AB} \sim 24-27$, 5σ completeness limit) ≥10-band imaging spanning from the observed-frame ultraviolet (UV) to the near-infrared (NIR) in addition to imaging data that span a variety of other wavelengths that are generally not used in this study. For the CFHTLS-D1 field we use the UV/optical/NIR imaging data described in Lemaux et al. (2014a,b). These data include deep ground-based $u^*g'r'i'z'$ imaging with the Canada-France-Hawai'i Telescope (CFHT)/MegaCam (Boulade et al. 2003) as part of the CFHTLS, as well as deep JHK_s imaging in the NIR from WIRCam (Puget et al. 2004) taken for the WIRCam Deep Survey (WIRDS; Bielby et al. 2012) and [3.6][4.5] μm imaging from the InfraRed Array Camera (IRAC; Fazio et al. 2004) on board the *Spitzer* Space Telescope taken as part of the *Spitzer* Extragalactic Representative Volume Survey (SERVS; Mauduit et al. 2012).

For the ECDFS field, we draw on the imaging data described in Cardamone et al. (2010) and references therein. These data include deep $UBVRIz$ imaging taken from the Garching-Bonn Deep Survey (GaBoDS; Hildebrandt et al. 2006) and the Multiwavelength Survey by Yale-Chile (MUSYC; Gawiser et al. 2006), as well as deep imaging in the NIR (JHK[3.6][4.5][5.8][8.0]) from MUSYC, Moy et al. (2003), and the Spitzer IRAC/MUSYC Public Legacy Survey in the Extended CDF-South (SIMPLE; Damen et al. 2011). Though this field is covered by *Hubble* Space Telescope (HST) observations with the Cosmic Assembly Near-infrared Deep Extragalactic Legacy Survey (CANDELS; Grogin et al. 2011; Koekemoer et al. 2011), only a subsection of the area that is spanned by the spectroscopic data used in this study is covered by these observations. Moreover, we have found that none of the physical parameters presented in this study (see Sect. 2.3) are, on bulk, appreciably affected by fitting to the deeper CANDELS data as opposed to the primarily ground-based imaging of Cardamone et al. (2010)[2].

For the COSMOS field we draw on two different data sets, which are described in detail in Lemaux et al. (2018). For the vast majority of the objects studied in this paper we use the "COSMOS2015" imaging data compiled by Laigle et al. (2016), which include imaging in the near-ultraviolet (NUV) from the GALaxy Evolution eXplorer (GALEX; Martin et al. 2005), ground-based $u^*BVri^+z^{++}$ UV/optical imaging from CFHT/MegaCam and Subaru/Suprime-Cam (Miyazaki et al. 2002), ground-based $YJHK$ imaging from Subaru/Hyper-Suprime-Cam (HSC, Miyazaki et al. 2012), the UltraVISTA survey (McCracken et al. 2012), and CFHT/WIRCam, as well as extremely deep [3.6][4.5][5.8][8.0] imaging from *Spitzer*/IRAC. All galaxies in our COSMOS spectroscopic sample (see Sect. 2.2) were matched to the COSMOS2015 catalog using nearest-neighbor matching with a maximum radius of 0.75″ (median offset 0.07″). For the small subset of galaxies with secure spectroscopic redshifts (hereafter $z_{\rm spec}$, see Sect. 2.2 for the operational definition of this phrase) in the COSMOS field for which we were not able to find a photometric counterpart in the COSMOS2015 catalog, we used v2.0 of the photometric catalog presented in Capak et al. (2007)[3], which uses a subset of the imaging in the COSMOS2015. For those objects that had counterparts in both catalogs, we noticed no systematic offset between parameters derived using the two different sets of photometry for any of the parameters presented in this study. Further details on these observations, their reduction, source detection, and magnitude measurements including point spread function (PSF) homogenization and the various methods used to apply aperture corrections can be found in Lemaux et al. (2014a,b), Cardamone et al. (2010), Capak et al. (2007), Laigle et al. (2016) and references therein.

2.2. Spectroscopic data

The spectroscopic data employed in this study were drawn from a variety of different surveys. For all redshift surveys we selected only those galaxies with secure $z_{\rm spec}$ measurements, the definition of which differs slightly based on the survey being used, and limited the redshift range to $2 < z_{\rm spec} < 5$. The majority of our $z_{\rm spec}$ values (53.7%) were taken from VUDS. This survey primarily utilizes photometric redshifts (hereafter $z_{\rm phot}$) drawn from the photometric catalogs described above[4] to select targets for spectroscopic follow up using VIMOS (Le Fèvre et al. 2003) mounted on the Nasmyth platform of the 8.2-m Very Large Telescope (VLT) Unit Telescope 2 (UT2/Melipal) at Cerro Paranal. The spectroscopic targets are largely limited to $i'/i^+/I < 25$ and those objects whose primary or secondary $z_{\rm phot}$ solution satisfies $z_{\rm phot} + 1\sigma > 2.4$. Spectroscopic observations consisted of approximately 50 400s of integration across the wavelength range $3650 \leq \lambda_{\rm obs} \leq 9350$ Å at a spectral resolution of $R = 230$. Further discussion of the survey design, observations, reduction, redshift determination, and the properties of the full VUDS sample can be found in Le Fèvre et al. (2015). Details of the first VUDS data release[5] can be found in Tasca et al. (2017).

The flagging code for VUDS is discussed in Le Fèvre et al. (2015). We take two different approaches regarding galaxies with different flags in this paper. For the selection of our sample as well as spectral energy distribution (SED) fitting, we consider those galaxies with flags = $X2, X3, X4$, and $X9$ as being "secure", where $X = 0$, 2, or 3[6]. According to Le Fèvre et al. (2015),

[2] More specifically we find a median difference of only 0.09 and 0.02 dex for stellar mass and SFR, respectively, for galaxies that are detected in both catalogs, with fitting run on MUSYC photometry generally returning larger values.

[3] Different detection bands and photometric masking methods resulted in some objects being present in the Capak et al. (2007) catalog that are not in the COSMOS2015 catalog. As in Lemaux et al. (2018), we exclude the *Spitzer*/IRAC cryogenic bands ([5.8]/[8.0]) presented in the Capak et al. (2007) catalog from all analysis.

[4] Because the COSMOS2015 catalog was not available at the inception of the VUDS survey, the Capak et al. (2007) photometry was used to measure $z_{\rm phot}$ values.

[5] http://cesam.lam.fr/vuds/DR1/

[6] $X = 0$ is reserved for target galaxies, $X = 2$ for non-targeted objects that fell serendipitously on a slit at a spatial location separable from the target, and $X = 3$ for non-targeted objects that were serendipitously subtended slit at the same spatial location as the target. Galaxies identified spectroscopically as broadline active galactic nuclei, $X = 1$ in the VUDS flagging system, are excluded from our analysis, due to the difficulty of measuring their physical parameters through spectral energy distribution fitting with the standard approach taken in this study. For more details on the fiducial probability of a correct redshift for a given flag, see Le Fèvre et al. (2015)

galaxies with these flags have a redshift that is reliable at the 75–99.3% level. In Sect. 2.4 we quantify the reliability of the different flags for VUDS and in the remaining part of our analysis that employs $z_{\rm spec}$ measurements, the creation of our metric of environment, the $z_{\rm spec}$ value for galaxies of differing flags are treated probabilistically using these reliability estimates.

The next largest contribution to our sample falls in the COSMOS field and is drawn from the Bright and Deep phases of the zCOSMOS survey (Lilly et al. 2007, 2009, and in prep.; Diener et al. 2013, 2015). The galaxies drawn from these surveys contribute 26.1% of our total sample. In the COSMOS field, a small number of additional redshifts were taken from Casey et al. (2015), Chiang et al. (2015), and Diener et al. (2015) at $z \sim 2.5$. In the ECDFS field, a list of publicly available redshifts was compiled by one of the authors (NPH) taken from a variety of different surveys (e.g., Vanzella et al. 2008, 2009; Hathi et al. 2009; Straughn et al. 2009; Balestra et al. 2010; Cooper et al. 2012; Kurk et al. 2013; Trump et al. 2013; Morris et al. 2015) and contribute 13.2% to our total sample. In the CFHTLS-D1 field, galaxies were drawn from the Deep and UltraDeep phases of the VVDS (Le Fèvre et al. 2005, 2013) and contributed 6.0% to our total sample. For each survey listed here we attempted as best as we were able to homogenize the flagging system relative to the VUDS flagging system and select only those galaxies that had flags equivalent to those considered secure for VUDS[7]. All galaxies observed in two or more surveys were assigned a single redshift based on the $z_{\rm spec}$ with the highest confidence flag, with VUDS redshifts being used in the case of a tie. A comparison of duplicate observations where at least one of those observations yielded a spectrum with a flag of $X3$ or $X4$ resulted in similar reliability statistics to those stated in Sect. 3.3 of Le Fèvre et al. (2015) for flags $X1$, $X2/X9$, and $X3/X4$.

Finally, we incorporate new follow-up DEIMOS (Faber et al. 2003) observations of the PCl J1001+0220 $z \sim 4.57$ proto-cluster located in the COSMOS field (Lemaux et al. 2018). These observations are part of the Charting Cluster Construction with VUDS and ORELSE (C3VO) survey, an ongoing campaign that involves observations with both DEIMOS and the Multi-Object Spectrometer For Infra-Red Exploration (MOSFIRE; McLean et al. 2012) on the Keck I/II telescopes. The Keck component of the C3VO survey is designed to provide a nearly complete mapping of the five most significant overdensities detected in VUDS, including those reported in Lemaux et al. (2014b, 2018), Cucciati et al. (2014, 2018), by targeting star-forming galaxies of all types to $i_{\rm AB} < 25.3$ (or $\sim L^*_{\rm FUV}$ at $z \sim 4.5$ and $< L^*_{\rm FUV}$ at $z \sim 2.5$) and Lyman-α (hereafter Lyα) emitting galaxies to fainter magnitudes.

The Keck-C3VO sample presented here comprises galaxies from the only two DEIMOS slitmasks that have been fully observed and analyzed at the time of writing. Including these observations allowed us to bolster the high-redshift end of our sample appreciably, as ∼10% of our high-z ($z > 4$) galaxy sample are Keck/DEIMOS galaxies. These observations additionally allowed us to populate the sample of galaxies in high-density environments at these redshifts more fully, as 20 new members of PCl J1001+0220 were discovered by these observations, which results in a combined sample that is more than triple the previously known member sample and provides an appreciable fraction (∼20%) of the high-z, high-density sample ($\log(1 + \delta_{\rm gal}) > 0.22$, see Sect. 2.4) presented in this work[8] The two DEIMOS masks included here were observed on December 22, 2016, and December 26, 2017, for ∼4 h each under nearly photometric conditions and 0.7–0.8″ seeing. For each mask we used the 600 l mm^{-1} grating in conjunction with the GG455 order blocking filter and a central wavelength of $\lambda_{\rm c} = 7200$ Å. All slitmasks were milled with 1″-wide slits. This setup resulted in a plate scale of 0.66 Å pix^{-1}, an $R \sim 2500$ ($R = \lambda/\theta_{\rm FWHM}$, where $\theta_{\rm FWHM}$ is the full-width half-maximum resolution), and a wavelength coverage of 4600 Å $\lesssim \lambda \lesssim$ 9800 Å. The two masks were centered at $[\alpha_{\rm J2000}, \delta_{\rm J2000}] = [10{:}01{:}02.25, 2{:}17{:}20.0]$ and $[10{:}01{:}22.92, 2{:}21{:}41.6]$ with a position angle of 90°, thus subtending a considerable fraction of the proto-cluster area as defined in Lemaux et al. (2018) (see Fig. 1 for the layout of these observations).

Targets were selected using a combination of magnitude and $z_{\rm phot}$ cuts. Primary targets were selected using the criteria $4.53 - 1\sigma_{\Delta z/(1+z)}(1 + z_{\rm PCl}) \leq z_{\rm phot} \leq 4.60 + 1\sigma_{\Delta z/(1+z)}(1 + z_{\rm PCl})$ and $i_{\rm AB} < 25.3$, where $z_{\rm PCl} = 4.57$, the systemic redshift of PCl J1001+0220, and $\sigma_{\Delta z/(1+z)} = 0.016$, which is a rough estimate of the photometric redshift precision in COSMOS at these redshifts. We note that this value of $\sigma_{\Delta z/(1+z)}$ was based on analysis presented in Smolčić et al. (2017a) using a different sample selection and methodology than that used for the full sample in this paper. It is considerably smaller than the equivalent value estimated using our sample (see Sect. 2.3), though, in practice, this discrepancy did not meaningfully affect our target selection process as primary targets were always subdominant on the DEIMOS masks due to their relatively low surface density resulting from the choice of $\sigma_{\Delta z/(1+z)}$. As such, lower priority targets were accommodated on our masks with relative ease, which included true member galaxies that were relegated to lower priority targets due to the restrictive $z_{\rm phot}$ cut used to select primary targets.

Objects with detections in X-ray and/or radio imaging at any $z_{\rm phot}$ value that lacked a secure $z_{\rm spec}$ were highly prioritized. Lower priority targets included objects in a similar magnitude range but within a larger $z_{\rm phot}$ range centered on the systemic redshift of PCl J1001+0220, objects in the same $z_{\rm phot}$ range but at fainter magnitudes ($25.3 < i_{\rm AB} \leq 26.5$), brighter objects ($i_{\rm AB} < 25.3$) likely in the background of the proto-cluster, and galaxies previously targeted by VUDS. These magnitude limits were imposed such that continuum observations at modest signal-to-noise ratios (S/N) of ∼1 per native resolution element could be achieved for our primary target sample such that redshifts were obtainable in the presence or absence of Lyα in emission.

Redshifts were evaluated with a modified version of the `zspec` code (Newman et al. 2013) which incorporated empirical high-redshift galaxy templates from the VUDS and VVDS surveys as well as high-resolution empirical Lyα templates from Lemaux et al. (2009). Each object inspected was assigned a quality code, Q, broadly following the convention of Newman et al. (2013). The one modification made to this convention was to assign a secure redshift ($Q = 3$) to those galaxies that exhibited a single redward skewed emission line indicative of Lyα, In total 256 objects were targeted across the two masks, yielding 73 high-quality redshifts, of which 50 were in the redshift range $4 < z < 5$. In addition, 25 high-quality redshifts were obtained for objects that serendipitously fell on the otherwise

[7] Broadly, the statistics of the flagging system in the zCOSMOS and VVDS surveys are on the same basis as those in VUDS making this task trivial for the bulk of these galaxies.

[8] In Sect. 3.2 we state, however, that the trends seen in our analysis hold if the entire population of the PCl J1001+0220 proto-cluster, including the DEIMOS sample, is excluded and are, thus, not dominated by a single structure at high redshift.

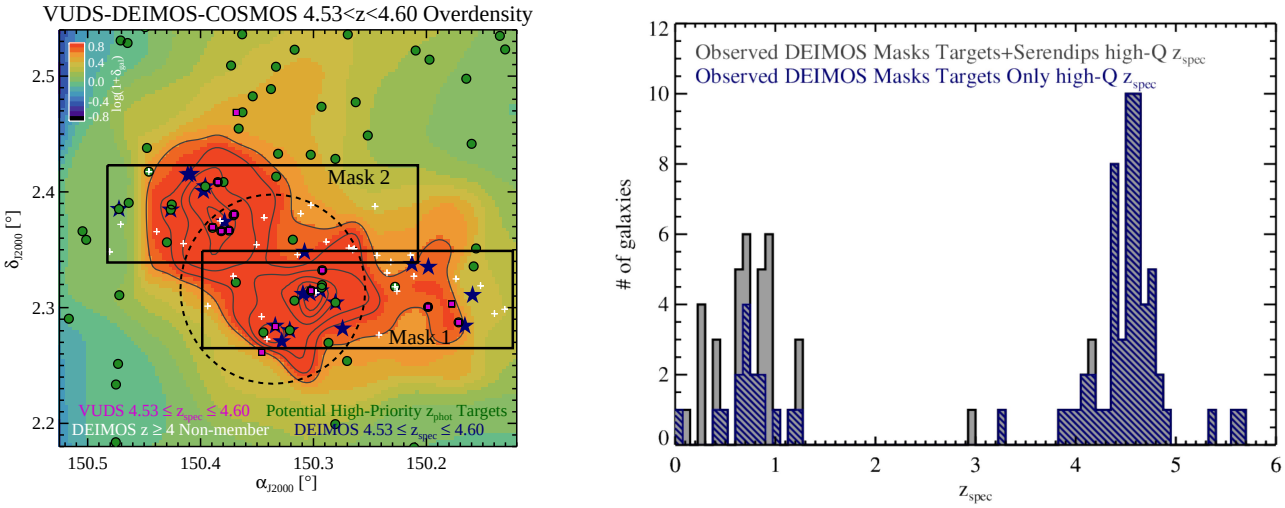

Fig. 1. View of the C3VO observations of the PCl J1001+0220 proto-cluster at $z \sim 4.57$. *Left*: layout of the two masks observed with DEIMOS as part of the C3VO survey in the vicinity of the PCl J1001+0220 proto-cluster against the backdrop of a two-dimensional overdensity map generated using the methodology described in Sect. 2.4, though here the overdensity is calculated over the entire redshift extent of PCl J1001+0220 indicated at the top of the plot. The two completed DEIMOS slitmasks are outlined in black. The dashed circle denotes $R_{\rm proj} = 2$ Mpc centered on the barycenter of the detection in the overdensity map. The highest priority DEIMOS targets ($i^+ < 25.3$ and $4.44 \leq z_{\rm phot} \leq 4.70$) in the vicinity of PCl J1001+0220 are shown as filled dark green circles. Galaxies with high-quality $z_{\rm spec}$ measurements from VUDS and from our new DEIMOS observations within the redshift range of PCl J1001+0220 are shown as purple squares and blue stars, respectively. Galaxies with high-quality $z_{\rm spec}$ measurements from the DEIMOS observations at $z > 4$ but not within the redshift range of PCl J1001+0220 are shown as white crosses. Galaxy overdensity contours indicate levels of ~3, 4, 5, 6, 7, 8$\sigma_{\rm NMAD}$ in excess of the background. *Right*: redshift histogram of all objects with secure $z_{\rm spec}$ measurements from Keck/DEIMOS observations. The blue hatched histogram shows the $z_{\rm spec}$ distribution of all targeted galaxies with a secure $z_{\rm spec}$, while the gray solid histogram also includes those galaxies that serendipitously fell on in the area subtended by the slits in the two masks. These DEIMOS observations add considerably to the high-redshift portion of the sample presented in this study, especially at the high-density end.

empty regions of our slits. These serendipitous detections were identified and extracted in the manner described in Lemaux et al. (2009). Figure 1 shows the spatial location of the two DEIMOS masks incorporated in this study, the locations of newly confirmed $z > 4$ galaxies, and the distribution of high-quality $z_{\rm spec}$ measurements on both masks.

Combining all samples together, removing duplicates, and imposing the NIR magnitude cuts that are used for each field to define the final sample both for photometric and spectroscopic objects (see Sect. 2.4), resulted in a total of 6730 galaxies with high-quality $z_{\rm spec}$ values. We note here, and will show later (see Sect. 2.5), that this sample is largely devoid of extremely dusty star-forming and quiescent galaxies, an issue that we will attempt to account for in later sections. This sample of 6730 galaxies will be referred to hereafter as the final VUDS+ spectral sample or simply the VUDS+ sample. We limit our main analysis to this purely spectroscopically selected sample of galaxies, rather than attempting to additionally include objects with photometric redshifts, as we cannot accurately or precisely assign environment measures to the latter population (see Sect. 2.4) given the large photometric redshift uncertainties at these redshifts. Additionally, uncertainties in estimates of galaxy parameters (see Sect. 2.3) for galaxies without a spectroscopic redshift do not incorporate the uncertainties in the photometric redshift, which is problematic for certain aspects of our analysis aimed at testing the robustness of the observed trends.

2.3. Synthetic model fitting

The photometry measured on the imaging observations described in the previous section was used as input for two different forms of SED fitting. In the first form of the SED fitting, aperture-uncorrected magnitudes were input to the code LE PHARE[9] (Arnouts et al. 1999; Ilbert et al. 2006, 2009) in order to determine $z_{\rm phot}$ values and associated probability density function (PDFs) for all sources detected in each field. The methodology used for computing $z_{\rm phot}$ follows that described in Ilbert et al. (2009, 2013), with the final $z_{\rm phot}$ for each object being derived from the median of the resultant PDFs, with their associated errors set by the 16th and 84th percentile of each PDF. The precision and accuracy of the $z_{\rm phot}$ estimates in each field over the redshift range $2 \leq z \leq 5$, at least as they are able to be measured by galaxies with secure $z_{\rm spec}$, are discussed in detail in Lemaux et al. (2014a, 2018, 2019), Smolčić et al. (2017a), Laigle et al. (2016). These numbers range from $\sigma_{\Delta z/(1+z)} = 0.032-0.035$ and $\eta = 20.2-26.3\%$, where η is the percentage of catastrophic outliers defined as $|z_{\rm spec} - z_{\rm phot}|/(1+z_{\rm spec}) > 0.15$, with no appreciable bias for a sample limited to $2 < z_{\rm spec} < 5$ and $K_s < 24.1/[3.6] < 23.1$, $[3.6] < 24.8$, and $[3.6] < 25.3$ in the CFHTLS-D1, ECDFS, and COSMOS fields, respectively (see Sect. 2.4 for the meaning behind these photometric cuts). We note that these estimates are different than some previous estimates taken from the literature because of the differing spectroscopic sample, photometric cuts, and redshift range considered. The above numbers are provide only a broad view of the quality of the photometric redshifts in each field, and it is rather through use of the reconstructed PDF for each individual $z_{\rm phot}$ object that the precision and accuracy of the $z_{\rm phot}$ measurements manifest themselves statistically in our analysis (see Sect. 2.4).

The second form of the SED fitting used the aperture corrected "total" magnitudes as input to LE PHARE in order to estimate physical parameters of the sample. For the purposes of this

[9] http://cfht.hawaii.edu/~arnouts/LEPHARE/lephare.html

paper, we used only the fitting for those galaxies with a secure $z_{\rm spec}$. For these galaxies, the redshift was fixed to the spectral redshift prior to fitting. Input photometry was fit to a variety of different Bruzual & Charlot (2003) synthetic models generated from exponentially declining and delayed star-formation histories (SFHs) using a Chabrier (2003) initial mass function (IMF) and varying dust contents and stellar-phase metallicities. More details on this fitting, including the parameter set used and a brief comparison to an alternative approach, can be found in Sect. 2.3.1. For each galaxy, the median of the marginalized PDF for each physical parameter was adopted as the value of that parameter, with the formal uncertainty adopted from the values of each parameter at the 16th and 84th percentile of the PDF.

We note that while SED-fit SFRs have considerable associated uncertainties, they are found to correlate well, on average, with independent measures of SFRs at intermediate and high redshift, at least for galaxies with SFRs in the range $5 \lesssim \mathrm{SFR} \lesssim 200\,M_{\odot}\,\mathrm{yr}^{-1}$ (e.g., Wuyts et al. 2011; Mostek et al. 2012; Arnouts et al. 2013; Rodighiero et al. 2014; Talia et al. 2015; Shivaei et al. 2016; Schaerer et al. 2020, though see Lower et al. 2020 for an alternate view). These independent measures include extinction-corrected rest-frame optical recombination line strengths as well as far-infrared and radio measurements among others, all of which are considerably less subject to the extinction and SFH concerns that can bias for UV-to-NIR SED-fit SFRs. The SFR range quoted above encompasses the vast majority of our sample.

In addition, all of our analysis is robust to the statistical incorporation of the formal random uncertainties in the derived SFRs (see Sect. 3.1). This statement is only conclusive evidence of the robustness of our results if the error budget of our SED-fit SFR estimates is not dominated by systematics and the statistical errors from the SED fitting process are properly estimated from the SED fitting process. However, it is only if the misestimation of the statistical errors or if those systematics are a strong function of the true SFR or of environment that they would meaningfully modify any of the results presented in this study. Regarding the statistical errors, the marginalized SFR PDFs are consistent with independent error estimates, such as those employing a Monte Carlo approach (as in, e.g., Ryan et al. 2014; Strait et al. 2021), which lends credence to the efficacy of the method on an absolute scale irrespective of variables like dust content and environment. Regarding the systematics, it is unlikely the level of extinction has a strong effect for any galaxies other than those with the largest dust content (e.g., Rodighiero et al. 2014), a population that is mostly absent from our VUDS+ sample and one that we attempt to account for separately in Sect. 3.1. There is no a priori reason to believe that the accuracy of SED-fit SFRs is a function of environment.

Despite attempting to homogenize the data as much as possible, a few differences were noticed in the distributions of the SED-fit parameters from field to field likely due to issues of attempting to fit both different sets of filters as well as different treatment of the photometry for each of the various surveys (see Sect. 2.3.2). For the SED-fit parameters employed in this study, M_* and SFR, our full spectroscopic sample exhibited a median offset of $+0.03/+0.07$ dex and $-0.13/+0.14$ dex for the two parameters, respectively, for the ECDFS and CFHTLS-D1 fields, respectively, relative to the COSMOS field. The COSMOS field is chosen as a reference field because it is the largest of the three VUDS fields, and choosing it serves to mitigate sample variance and allows for the tests that are performed in Sect. 2.3.2. While it is possible this offset is physical and related to sample variance of the galaxy populations or differing selection functions across the different fields, this is not likely as a similar field-to-field offsets were seen in smaller redshift bins spanning the range of the full sample. The possibility that sample variance is primarily responsible for inducing these offsets is discussed further in Sect. 2.3.2.

We correct for this effect by subtracting the bulk offset observed in the ECDFS and CFHTLS-D1 fields from the individual M_* and SFR values of all galaxies in those fields. As the offsets were measured by comparing to the average values in the COSMOS field, average M_* and SFR values for the galaxies in the COSMOS field were unchanged by this process. These corrected values in the CFHTLS-D1 and ECDFS fields are used in all subsequent analysis. We note that none of the results in this paper are changed appreciably if we do not make this correction. Additionally, the main results also persist at a slightly reduced significance if we instead limit our sample to the COSMOS field that is uncorrected for this effect.

2.3.1. Details of the Le Phare spectral energy distribution fitting

In total, we employed seven different BC03 models for the Le Phare SED fitting, five with SFHs characterized by an exponentially decaying tau model of the form $\psi(t) \propto \tau^{-1} \mathrm{e}^{-t/\tau}$ and two delayed exponentially decaying tau models of the form $\psi(t) \propto \tau^{-2} t \mathrm{e}^{-t/\tau}$. All templates are considered at 43 possible ages between 50 Myr and 13.5 Gyr with the constraint that the age of the model fit to a given galaxy cannot be older than the age of the universe t_H at the redshift of that galaxy. The delayed tau models are included as it has been suggested that high-redshift galaxies have SFHs that may deviate considerably from the simple exponentially decaying tau models (e.g., Maraston et al. 2010; Schaerer et al. 2013). Values of τ range from 0.1 to 30 Gyr in roughly logarithmically equal time steps and delay times are set to 1 and 3 Gyr. Each BC03 model employs a Chabrier (2003) initial mass function and two values of stellar-phase metallicity, 0.4 $Z_{\odot}$ and $Z_{\odot}$. Stellar extinction is allowed to vary between $E_{\rm s}(B-V) = 0$ and 0.5 in steps of 0.05, with the prescription also allowed to vary between the Calzetti et al. (2000) starburst law and a Small Magellanic Cloud-like law (Prévot et al. 1984; Arnouts et al. 2013). Several prominent nebular emission lines are also added to the templates following the methodology of Ilbert et al. (2009). The median of the marginalized PDF for each parameter for each galaxy was adopted as the parameter value, with the uncertainties set by the 16th/84th percentile of the marginalized PDF. We note that, for this fitting, we only used the broadbands available in each field to perform the fitting in order to homogenize the photometric constraints as much as possible across the three fields, while for the photometric redshift estimation all available bands (i.e., medium and broadbands) were used.

We compared the values of M_* and SFR estimated by our Le Phare fitting to those estimated using the Code Investigating GALaxy Emission (CIGALE; Burgarella et al. 2005; Noll et al. 2009; Boquien et al. 2019)[10] imposing an identical parameter space to that employed in the Le Phare fitting to the best of our ability given the large differences in the codes. We also tested the effects of including and excluding various bands for subsets of our sample in the COSMOS field at various redshifts (Staab et al., in prep.). Despite the dramatically different approach taken by CIGALE, we found no appreciable bias between the M_* and SFR values estimated by CIGALE using all bands available for

[10] https://cigale.lam.fr/

COSMOS and those estimated by LE PHARE using only the broadbands, with an ∼0.2 dex scatter for each parameter.

2.3.2. The dependence of physical parameter offsets on sample variance

As discussed in Sect. 2.3, the median values of M_* and SFR estimated for galaxies in the three fields studied in this paper varied. Specifically, for our full spectroscopic sample, there was an offset of +0.03/+0.07 dex and −0.13/+0.14 dex for M_* and SFR, respectively, for galaxies in the ECDFS and CFHTLS-D1 field, respectively, relative to those in the COSMOS field. In this section, we investigate whether these differences may be due to sample variance effects.

The coverage of our spectral data is the largest in the COSMOS field out of the three fields studied here, with the coverage being roughly two and five times the size of the CFHTLS-D1 and ECDFS fields, respectively. Since all photometric data in an individual field is treated in a homogenized manner, we can test the ability of sample variance alone to reproduce the offsets seen in the M_* and SFR values for the average galaxy in the CFHTLS-D1 and ECDFS fields by sub-sampling the COSMOS data in regions that are of equivalent sizes to these two fields. To this end, we broke the spectral sample in the COSMOS field into separate contiguous areas containing roughly equal numbers of galaxies and calculated the dispersion of the median M_* and SFR values in the different regions. This exercise was performed for two, three, four, five, and six separate regions. The maximum dispersion in this method was 0.04 dex in both parameters, which is less than most of the field-to-field offsets measured in Sect. 2.3.

It is also possible that the heterogeneous selection of galaxies within our final VUDS+ sample could contribute to the observed offsets. The VUDS survey was selected nearly exclusively through a homogeneous set of $z_{\rm phot}$ or color criteria across all fields. If selection effects were the primary reason for the observed offset, we should see offsets that are considerably smaller if only the VUDS galaxies are considered for each fields. However, the median offsets from field to field in both parameters are nearly identical to those of the full VUDS+ sample. We conclude from these exercises that the observed offsets are unlikely due to sample variance or selection effects, and are rather primarily an artifact of the heterogeneous imaging observations and treatment of the photometric data across the various fields. None of the results presented in this paper change meaningfully whether or not the observed offsets in M_* and SFR are applied to the galaxies in the non-COSMOS fields.

2.4. Local environment

To define environment in this study we rely on a modified version of the Voronoi tessellation measure of the density field that has been employed by a variety of other studies that rely nearly exclusively on photometric redshifts (e.g., Scoville et al. 2013; Darvish et al. 2015; Smolčić et al. 2017a). The method used here, known as Voronoi Monte Carlo (VMC) mapping, which uses a weighted combination of spectroscopic and photometric redshift information, follows the method described in Lemaux et al. (2018) almost identically. As such, it is only briefly described here. For each field, beginning at $z = 2$ and reaching up to $z \sim 5$ in steps of 3.75 Mpc steps along the line of sight, a suite of 25 Monte Carlo realizations of $z_{\rm spec}$ and $z_{\rm phot}$ catalogs were generated for each step. As in other studies employing the VMC mapping at high redshift (Cucciati et al. 2018; Lemaux et al. 2018), the $z_{\rm spec}$ values are not considered as absolute truth, but are rather treated statistically following the method outlined in Appendix A. At each iteration of each step, a set of objects with and without $z_{\rm spec}$ values were defined following the method described in Appendix A. The spectral and photometric sample realized for a given iteration and slice was then cut at a magnitude limit that was determined uniquely for each field, [3.6] < 25.3 for COSMOS, [3.6] < 24.8 for ECDFS, and [3.6] < 23.1 and K_s < 24.1 for CFHTLS-D1. Detection in two NIR bands was required for the CFHTLS-D1 field due to the relative shallowness of the IRAC imaging in this field and the slightly different approach taken for measuring IRAC photometry (see Le Fèvre et al. 2015). This requirement is not imposed in the other two fields, as the ground-based NIR data were shallower than the IRAC imaging in those fields. As a consequence, for the COSMOS and ECDFS field, the [3.6] cut effectively guaranteed useful information in the other NIR bands, which ensured that the rest-frame SED of all sources was meaningfully probed over the Balmer/D_n(4000) break. These photometric limits correspond to the 3σ limiting depth of the IRAC/WIRCam images in the three fields[11]. Since these bands probe light redward of the Balmer/4000 Å break for the redshifts considered here, the tracer populations used to estimate the local density can be considered to be broadly stellar mass limited[12]. Adopting the methodology used by several other works (Quadri et al. 2012; Tomczak et al. 2014; Lemaux et al. 2018, see Appendix B of Lemaux et al. 2018 for a description of the method), we estimate that the resultant sample after imposing these cuts is 80% complete to $\log(M_*/M_\odot) \sim 9.2$–$9.5$ across the three fields at $z \sim 3$, with the exact limit depending on the NIR imaging data available in a particular field. These estimates are quoted primarily to provide a rough characterization of the tracer population used in the reconstruction of the density field in order to ease comparison with other works.

For each realization of each redshift step, two-dimensional Voronoi tessellation is then performed on all objects whose assigned redshift fell within ±3.75 Mpc of the central redshift of each bin, in other words, a bin width of $\Delta\chi = 7.5$ Mpc or $\Delta z \sim 0.015$–0.08 from $z \sim 2$–5. The 3.75 Mpc steps between slices along with the slice thickness ensure overlap between successive slices such that we do not miss overdensities by randomly choosing unlucky redshift bounds. For each realization of each slice, a grid of 75 × 75 kpc pixels was created to sample the underlying local density distribution. The local density at each grid value for each realization and slice was set equal to the inverse of the Voronoi cell area (multiplied by $D_{\rm A}^2$, where $D_{\rm A}$ is the angular diameter distance at the redshift of interest) of the cell that enclosed the central point of each pixel. Final local densities, $\Sigma_{\rm VMC}$, for each grid point in each redshift slice are then computed by median combining the values of 25 realizations of the Voronoi maps. The choice of 25 realizations was motivated by balancing computational time with a sufficient

[11] We note that overdensity values in a given field are not a strong function of the precise magnitude cut imposed. For example, adopting a [3.6] < 24.8 cut in the COSMOS field, the same cut as was used for ECDFS, does not result in a larger scatter or bias relative to the fiducial map as simply rerunning the VMC mapping at the same magnitude limit.

[12] As an example, in the COSMOS photometric and spectroscopic sample employed in our analysis, the rest-frame dust-uncorrected absolute i-band magnitude, a band that is roughly equivalent to observed frame [3.6] at $z \sim 4$, has a Spearman rank correlation coefficient, ρ, of −0.88 and −0.91, respectively, with a $\gg 3\sigma$ rejection of the null hypothesis that the two parameters are uncorrelated.

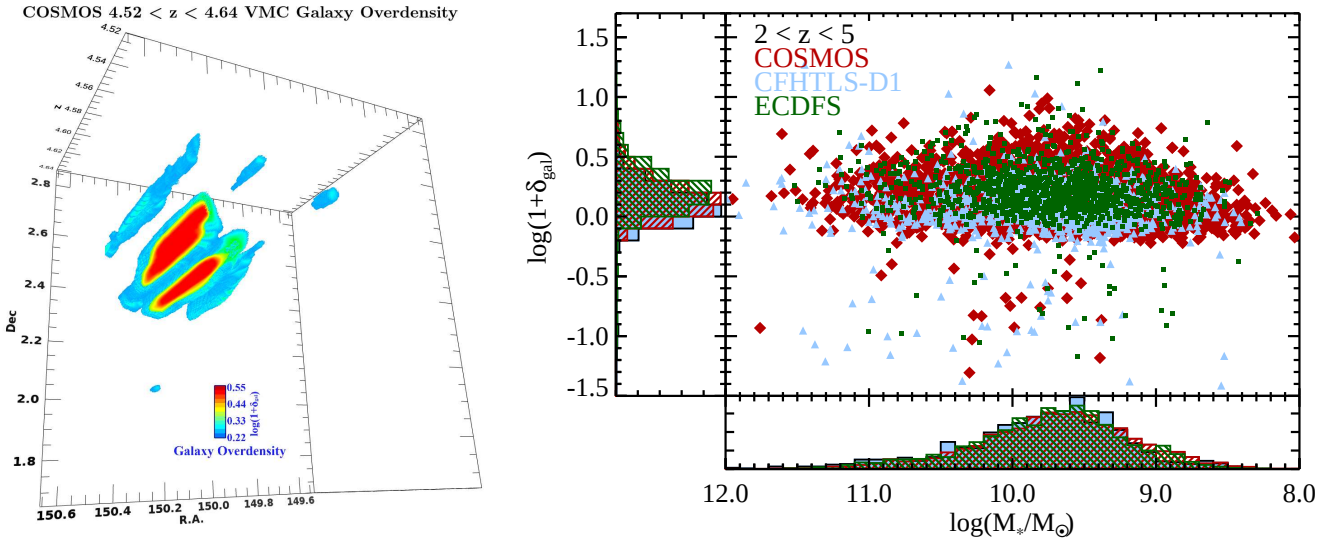

Fig. 2. Galaxy overdensity reconstruction using the VMC mapping method. *Left*: example of our VMC overdensity mapping (see Sect. 2.4) as applied to the COSMOS field in the redshift range $4.52 \leq z \leq 4.64$, nearly an identical range as is shown in Fig. 1. The main structure seen in the mapping is again the PCl J1001+0220 proto-cluster at $z \sim 4.57$. Here, in addition to showing the transverse dimensions, we also show the extent of the structure in the third dimension, redshift, which extends in this cube between $4.52 \leq z \leq 4.64$. The redshift dimension is added by rendering the narrow redshift slices used in our analysis to define galaxy overdensity rather than employing a single slice over the redshift extent of the proto-cluster as was done in Fig. 1. The scale bar in the lower right shows the galaxy overdensity values, with the lower and upper end of the dynamic range corresponding the "Intermediate" and "Peak" regions as defined in Sect. 3.1. *Right*: distribution of the full VUDS+ spectral sample in M_* and $\log(1+\delta_{\rm gal})$ for the three separate fields targeted by VUDS (ECDFS: small green squares, CFHTLS-D1: light blue triangles, COSMOS: large red diamonds). The redshift range imposed on the plotted galaxies is shown in the top left. Area-normalized histograms for the three fields for both parameters are shown on the side of the plot. The three fields show generally similar distributions in both parameters, with a slight excess of galaxies at higher $\log(1+\delta_{\rm gal})$ observed in COSMOS and ECDFS.

number of realizations to effectively sample the probability distributions of the $z_{\rm phot}$ and $z_{\rm spec}$ objects. In previous tests used for the $z \sim 1$ version of this mapping (see, e.g., Lemaux et al. 2017; Tomczak et al. 2017; Hung et al. 2020) where the computational time to generate maps is considerably less, maps that were created using 25 iterations did not show significantly higher variance in their density values relative to different realizations of maps using two or four times more iterations.

The local overdensity value for each grid point is then computed as $\log(1+\delta_{\rm gal}) \equiv \log(1+(\Sigma_{\rm VMC}-\tilde{\Sigma}_{\rm VMC})/\tilde{\Sigma}_{\rm VMC})$, where $\tilde{\Sigma}_{\rm VMC}$ is the median $\Sigma_{\rm VMC}$ for all grid points over which the map was defined (i.e., excluding an $\sim$1′ wide border region to mitigate edge effects)[13]. Uncertainties on the $\log(1+\delta_{\rm gal})$ values of each pixel are taken from the 16th and 84th percentile of the distribution of $\log(1+\delta_{\rm gal})$ values populated by the 25 realizations (i.e., the fourth lowest and highest $\log(1+\delta_{\rm gal})$ value for all realizations). Because these maps are, generally, so large in the transverse dimensions relative to the size of any contained structures, the maps are much less sensitive to the types of issues discussed in previous works that implement the VMC method (e.g., Cucciati et al. 2018; Hung et al. 2020) that serve to confuse or bias overdensity measurements in certain redshift slices due to the presence of large structures (i.e., if a given structure is near the size of the field, the median $\Sigma_{\rm VMC}$ value for that slice will be artificially increased causing an overall decrease in the density contrast, $\delta_{\rm gal}$, for that structure). The use of a NIR-selected sample rather than an optically selected sample also serves to mitigate these issues, as, due to the higher source density at a fixed magnitude limit, a larger fraction of $z_{\rm phot}$ objects enter into each VMC map, which serves to smooth out the density field. As such, it was not necessary to take the approach used in Cucciati et al. (2018) and Hung et al. (2020) to fit the average density value and root mean squared (rms) fluctuations as a function of redshift slice. Rather, here we simply use the median density value measured on the masked maps to calculate $\log(1+\delta_{\rm gal})$. Using the approach adopted in Cucciati et al. (2018) and Hung et al. (2020), while only subtly different than the one used here, is crucial when attempting to search for coherent overdensities, such as (proto-)groups and clusters, to define the global environment of galaxies. This approach will be used to define this environmental metric in future work presenting the full set of overdensity candidates in the VUDS+ sample. We note that adopting this approach has no meaningful consequences for the results presented in this paper.

The main modification to the VMC method made in this work relative to other works that employ this technique is the formalism of the statistical treatment of the spectral redshifts in the mapping. This modification is described in Appendix A. In Fig. 2 we show an example of our VMC reconstruction of a proto-cluster at $z \sim 4.57$ in the COSMOS field as well as the stellar mass versus. overdensity distribution of galaxies with secure $z_{\rm spec}$ values in each of the three fields. We note that all galaxies with an assigned overdensity value of $\log(1+\delta_{\rm gal}) < -0.3$ were removed from the final sample as such values are likely attributable to edge effects or other artifacts. Such galaxies constituted a negligible percentage of our original VUDS+ sample (<1%). Additionally, our results are not appreciably changed if we instead include these galaxies in the analysis nor if we slightly change the value at which we cut (i.e., ±0.1 dex in

[13] This is what we refer to as the masking procedure later in the section. Briefly, the masking procedure used for the maps disregards all pixels in the maps that have values below a certain value in each field that are calibrated for that particular field to exclude the regions where the spectral and photometric coverage begins to fall off. This masking is used only when calculating $\tilde{\Sigma}_{\rm VMC}$ for each VMC slice.

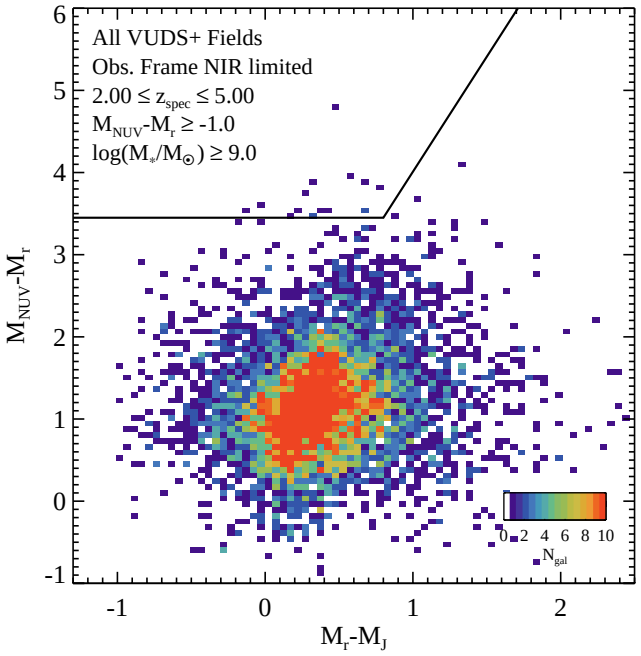

Fig. 3. Rest-frame $M_{NUV} - M_r$ vs. $M_r - M_J$ color–color diagram of the galaxies in the final spectral sample that satisfy the stellar mass, redshift, and $M_{NUV} - M_r$ limits given in the top left as well as the observed-frame NIR photometric cuts mentioned in Sect. 2.4. A color bar on the bottom right indicates the color that corresponds to the number of galaxies in each two-dimensional bin. The black lines delineate color-color regions that are inhabited by quiescent (*top left*) and star-forming (*bottom*) galaxies adopted from regions defined for a sample in a similar redshift in Lemaux et al. (2014b). The sample shown here is primarily composed of star-forming galaxies containing low to moderate amounts of dust.

$\log(1 + \delta_{\rm gal})$). As in the case of the SED fitting parameters, we noticed a slight variation in the median $\log(1+\delta_{\rm gal})$ values across the spectral sample in the three fields, with $\log(1 + \tilde{\delta}_{\rm gal}) = 0.14$, 0.11, and 0.20 in the COSMOS, CFHTLS-D1, and ECDFS fields, respectively[14]. However, these offsets were small and varied over the redshift range of the final spectral sample, which implied the genesis of the difference was perhaps astrophysical or due to a subtlety in the VMC map-making process, for example, different tracer populations, slightly different masking, the size of the field relative to the size of large-scale structure. Therefore, we decided not to apply corrections for this effect. As for the correction we made for the physical parameters in the previous section, we note here that the main results of this study are broadly invariant to whether or not we make a bulk correction for the differing $\log(1 + \delta_{\rm gal})$ values.

2.5. Representativeness of the spectral sample

In Fig. 3 we show the rest-frame $M_{NUV} - M_r$ vs. $M_r - M_J$ color–color diagram of all galaxies in the range $2 \leq z_{\rm spec} \leq 5$ subject to the observed-frame NIR magnitude cut discussed previously (see Sect. 2.4 for details on this cut for each field). Additionally, for this exercise we impose rest-frame color and stellar mass cuts to the sample of $M_{NUV} - M_r \geq -1$ and $\log(M_*/M_\odot) \geq 9$. These additional color and stellar mass cuts retain the vast majority (>90%) of the galaxies in the final spectral sample and are imposed because our imaging data are severely incomplete outside of these limits. Overplotted on this figure is the delineation line between regions that generally contain quiescent and star-forming galaxies. These regions are adopted from the regions estimated in Lemaux et al. (2014b) for galaxies in the redshift range $2 \leq z < 4$. The rest-frame colors of the galaxies in the full spectral sample are generally consistent with those of star-forming galaxies with minimal levels of extinction ($A_v < 1.5$).

That the majority of the galaxies in the final spectral sample appear at these rest-frame colors is perhaps problematic for leveraging this study into a general study of galaxy evolution. Though quiescent galaxies are by far a subdominant population over the redshift and stellar mass ranges plotted (e.g., Ilbert et al. 2013; Muzzin et al. 2013; Tomczak et al. 2014), such galaxies are observed to exist over this redshift range (e.g., Gobat et al. 2011; Cassata et al. 2013; Newman et al. 2014; Wang et al. 2016, 2018). Further, dusty star-forming galaxies, galaxies that are essentially completely absent from the spectral sample, also contribute to the overall galaxy population at these redshifts, particularly at the highest stellar masses (e.g., Casey et al. 2014, 2015; Lemaux et al. 2014b; Smolčić et al. 2017a,b). The contributions of each of these two populations will be considered separately when we investigate the SFR$-\log(1+\delta_{\rm gal})$ relation in earnest later in the paper. For now we consider only the question of whether or not the final VUDS+ spectral sample can be considered representative of the full population of non-dusty star-forming galaxies at $2 \leq z \leq 5$, a population that comprises the vast majority of the galaxy population in the early universe.

In Fig. 4 we show a $M_{NUV} - M_r$ vs. M_* color–stellar mass diagram. In the left panel of this figure, we show the density of the same spectral sample as was shown in Fig. 3 in color–stellar mass space. Overplotted contours indicate the density of the underlying sample of objects in the same $z_{\rm phot}$ range that are significantly detected at or above the 3σ limit of the NIR image appropriate for that field (i.e., the photometric parent sample) in the same space. The right panel of this figure directly compares the spectral sample with the photometric parent sample. In all cases we limit the sample to $\log(M_*/M_\odot) \geq 9$ and excise any galaxies with secure spectral redshifts that are outside the range considered here ($2 \leq z \leq 5$). Again, this stellar mass limit is imposed as our imaging data are severely incomplete below this limit, which precludes our ability to do the tests that follow. We chose to agnostically include galaxies below this stellar mass limit in our main analysis as, due to the lack of imaging depth, we cannot definitively prove or disprove whether the spectral sample below this limit is representative. However, the vast majority of galaxies in our $z_{\rm spec}$ sample are above this stellar mass limit, and our results do not change meaningfully if we instead exclude $z_{\rm spec}$ galaxies below this limit in all subsequent analysis.

While the left panel of Fig. 4 shows the number of galaxies in a given two-dimensional color/stellar mass bin, in the right panel the color bar indicates the fraction of $z_{\rm phot}$ objects in each bin that have a secure $z_{\rm spec}$. For objects in the $M_{NUV} - M_r$ and M_* range used to select the final spectral sample it is apparent that $\gtrsim$5% of objects in each color/stellar mass bin over which the majority of the photometric objects lie in this phase space (see the contours in the left panel of Fig. 4) have a secure $z_{\rm spec}$ except for the reddest objects, colors that are generally reserved for quiescent and dusty star-forming galaxies. The area normalized histograms for the $z_{\rm phot}$ and the final spectral sample generally appear to show a high degree of concordance. However, a deviation in the one-dimensional histograms is observed at the

[14] We note that $\log(1 + \tilde{\delta}_{\rm gal})$ is not zero since the value is always measured at the location of a galaxy, which is a denser region than typical in the universe.

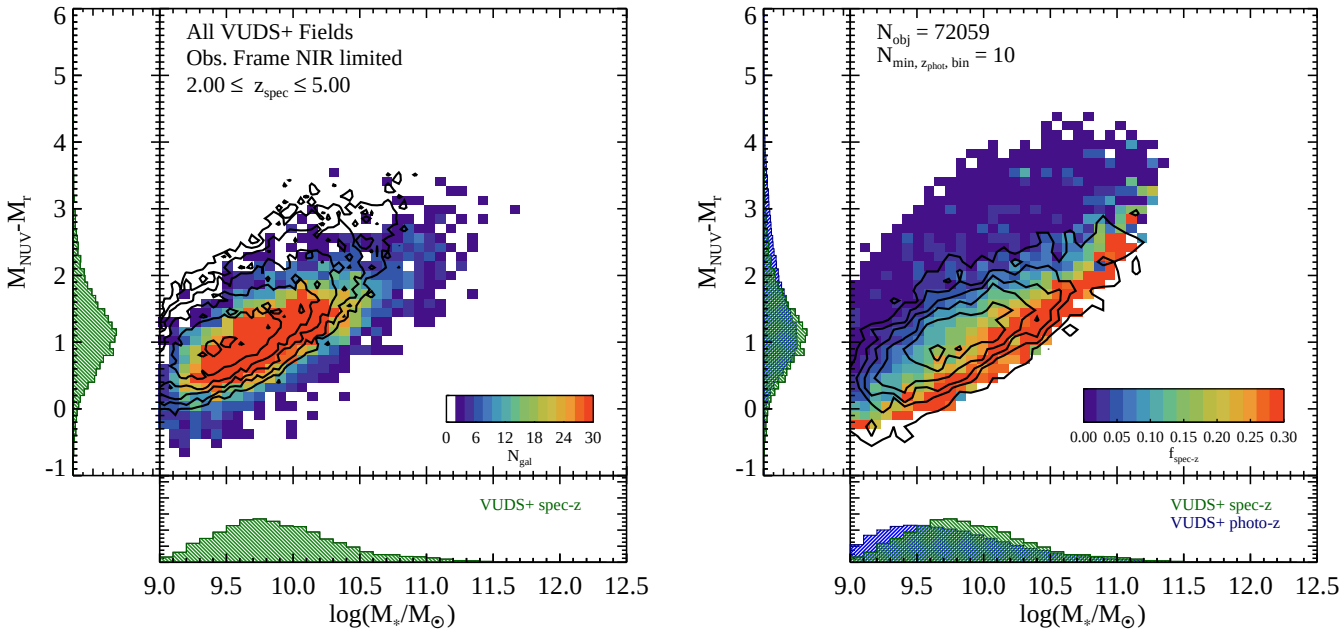

Fig. 4. Comparison of the VUDS+ spectroscopic sample and the underlying parent sample. *Left*: rest-frame color-stellar mass of of objects across all three VUDS fields in the range $2 \leq z_{\rm spec} \leq 5$ that have a secure spectroscopic redshift and meet the observed-frame NIR magnitude cuts discussed in Sect. 2.4. The color bar indicates the number of galaxies within each narrow color and stellar mass bin. Area-normalized histograms of color and stellar mass for the VUDS+ $z_{\rm spec}$ sample are shown on the sides of the plot. The contours indicate the density of the parent photometric sample in this space and are spaced in equal logarithmic steps of 0.2 dex starting at $N_{\rm phot} = 15$. The offset between the peak of the photometric and spectroscopic samples is ∼0.3 dex in stellar mass, with the photometric sample peaking at lower stellar masses. *Right*: same as the left panel, except the color bar now indicates the fraction of $z_{\rm phot}$ objects in each color and stellar mass bin that have secure spectral redshifts. The total number of photometric objects and the number of photometric objects required to fall in a two-dimensional bin in order for that bin to be plotted are indicated in the *top left*. Area normalized histograms of the full $z_{\rm phot}$ and VUDS+ $z_{\rm spec}$ sample are shown on the sides of the plot. The offset of ∼0.3 dex in stellar mass between the peak of the photometric and spectroscopic samples is also seen here, with the former peaking at lower stellar masses. The contours indicate the density of the spectral sample (i.e., the same as is shown in the left panel) and are spaced in equal logarithmic steps of 0.2 dex starting at $N_{\rm spec} = 5$.

lowest stellar masses plotted (i.e., $\log(M_*/M_\odot) \lesssim 9.5$), with an ∼0.3 dex offset observed between the peak of the stellar mass distribution of the photometric and spectroscopic samples. This deviation can also be seen in the two-dimensional density of the parent photometric and spectral sample in the left panel of Fig. 4. Above $\log(M_*/M_\odot \gtrsim 9.5)$, the two distributions are not meaningfully different, with a one-dimensional Kolmogorov–Smirnov (KS) test between the two samples at these masses returning no significant ($>3\sigma$) evidence to reject the null hypothesis that the two distributions are drawn from the same sample.

There also appears to be a clear selection effect present in the two-dimensional plot in which galaxies of redder colors have $z_{\rm spec}$ fractions lower than those of their bluer counterparts at a given stellar mass. While it is apparent from the contours overlaid on the right panel of Fig. 4 that the bulk of the galaxies within the spectral sample reside at intermediate rest-frame colors at a given M_*, it is still possible that the over-representation of bluer galaxies at a given M_* could subtlety bias our investigation of the relationship between SFR and $\delta_{\rm gal}$. As we will show in Sect. 3.3, this is likely not the case, as homogenizing the $z_{\rm spec}$ fraction for all color–M_* that are reasonably well sampled (see Sect. 3.3 for the precise definition of this term), yields results that are broadly unchanged from those using the full spectral sample. Additionally, we will show in Sect. 3 that our results are largely invariant when including the contribution of quiescent and dusty star-forming galaxies under a variety of different assumptions. Thus, we conclude that the lack of representativeness of our spectral sample does not meaningfully bias any of the results presented in this paper.

3. The evolution of the SFR-density relation

In the previous sections we have defined a sample of 6730 unique galaxies in the redshift range $2 < z_{\rm spec} < 5$ with estimates of M_*, SFR, and local environment, $\log(1+\delta_{\rm gal})$. For the remainder of the paper, we investigate the relationship of these parameters and the consequences of those relationships for environmentally driven galaxy evolution in the early universe. The galaxies in our final spectral sample, while not strictly representative of low to moderately dusty star-forming population at these redshifts, do not appear different from such galaxies in any way that is meaningful for the results that follow (see Sect. 3.3). Additionally, while quiescent and dusty star-forming galaxies are almost completely absent from this sample, we will show later that our main conclusions are robust to their absence. With those caveats in place, we begin by investigating the general relationship between SFR, M_*, and $\log(1+\delta_{\rm gal})$ in our final spectral sample.

3.1. The general SFR–density and M_*–density relations at high redshift

In the left panel of Fig. 5 we plot the relationship between SFR and $\log(1+\delta_{\rm gal})$ for the 6730 galaxies in our final VUDS+ sample over the full redshift range of the sample, $2 < z < 5$.

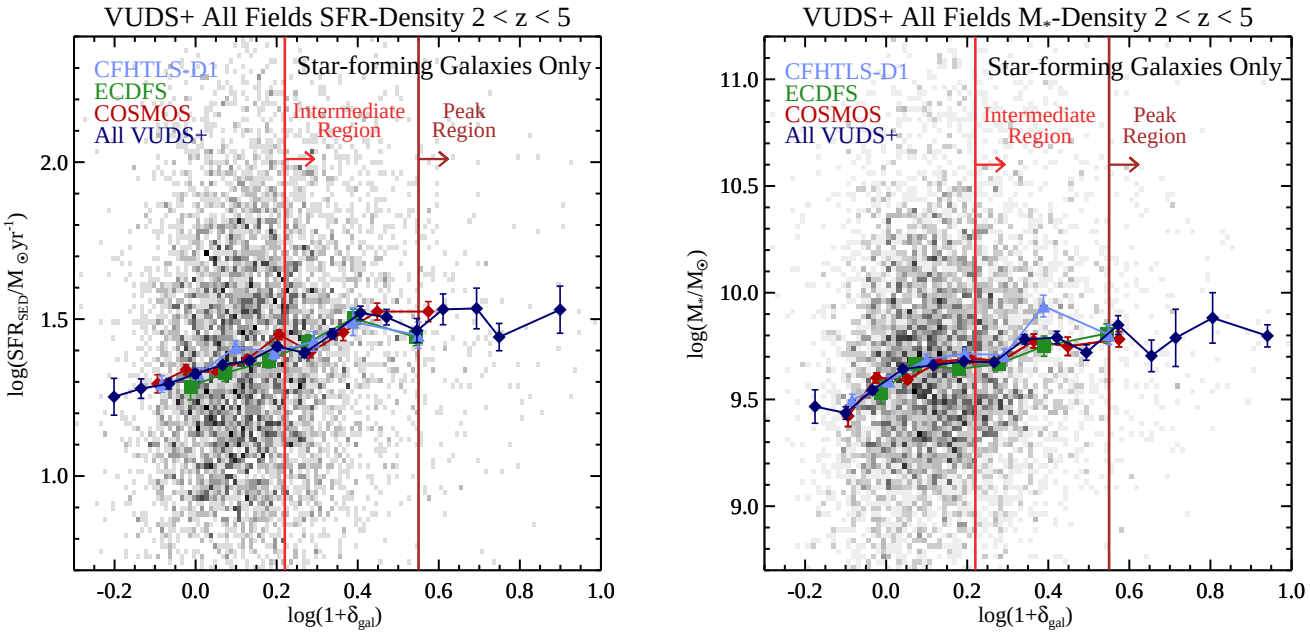

Fig. 5. Galaxy properties as a function of environment in the VUDS+ sample. *Left*: relationship between SFR and $\log(1+\delta_{\rm gal})$ for the 6730 galaxies in the VUDS+ spectroscopic sample. The backdrop shows the number density at a given SFR and $\log(1+\delta_{\rm gal})$ value for all galaxies in the sample and the light blue, green, red, and dark blue datapoints and lines show median values in each bin in $\log(1+\delta_{\rm gal})$ for galaxies in the CFHTLS-D1, ECDFS, COSMOS, and the full combined VUDS+ sample, respectively. Uncertainties reflect errors on the median values. The vertical dashed lines indicate the "Intermediate" and "Peak" regions of the $\log(1+\delta_{\rm gal})$ distributions (see Sect. 3.1), with all values lower than $\log(1+\delta_{\rm gal}) = 0.22$ being considered "Field" galaxies. The "All VUDS+" sample can be plotted over a larger dyanamic range in $\log(1+\delta_{\rm gal})$ relative to the individual field samples due to its larger sample size. A weak but highly significant positive correlation is observed (see Sect. 3.1). *Right*: as in the left panel, but now plotted for stellar mass (M_*) and $\log(1+\delta_{\rm gal})$. Again, a weak but highly significant positive correlation is observed between M_* and $\log(1+\delta_{\rm gal})$

The colored SFR and $\log(1+\delta_{\rm gal})$ points are plotted against the backdrop of the individual values for the full sample indicate the median SFR in bins of $\log(1+\delta_{\rm gal})$. The errors associated with each median value are calculated by the normalized median of the absolute deviations $\sigma_{\rm NMAD}/\sqrt{n-1}$ of the individual SFR values of each bin, where n is the number of galaxies in each bin (see Lemaux et al. 2018 and references therein for details on this error estimate). In addition, three different regions are demarcated in the plot, a Field region, defined as $\log(1+\delta_{\rm gal}) < 0.22$, an Intermediate region, defined as $0.22 \leq \log(1+\delta_{\rm gal}) < 0.55$, and a Peak region, defined as $\log(1+\delta_{\rm gal}) \geq 0.55$. The latter two of these regions are set to correspond to the outskirts and peak regions of the Hyperion proto-supercluster defined in Cucciati et al. (2018), and can more generally be thought of as the outskirts and the core region of the protocluster environment[15].

In stark contrast to what is observed at lower redshifts ($z < 2$), there exists a clear, nearly monotonic increase in the average SFR with increasing $\log(1+\delta_{\rm gal})$. This increase is observed to be ~0.3 dex in SFR over the full dynamic range of $\log(1+\delta_{\rm gal})$ probed by the sample ($-0.3 \leq \log(1+\delta_{\rm gal}) \leq 1$). This relation is also plotted for the subsamples that are drawn from the three individual fields and mirrors the behavior of the full VUDS+ sample without exception. The consistency of the relation across all three fields is important to lend credence to these results. To further formalize this result, we calculated the Spearman rank correlation coefficient, ρ, between SFR and $\log(1+\delta_{\rm gal})$ for the full VUDS+ sample, finding $\rho_{{\rm SFR}-\delta_{\rm gal}} = 0.13$, which indicates a weak but highly significant positive correlation, with a rejection of the null hypothesis of lack of correlation between the two variables at the $\sim 10\sigma$ level. We note that the Spearman coefficient was calculated on the individual data points in the full VUDS+ sample rather than the values in the binned data points shown in Fig. 5. This coefficient was also calculated for the COSMOS-only sample resulting in $\rho_{{\rm SFR}-\delta_{\rm gal}} = 0.15$ at only a slightly reduced significance ($\sim 8.5\sigma$). Within the VUDS+ data there is a clear reversal of the SFR–density (hereafter SFR$-\delta_{\rm gal}$) relation.

While it is tempting to interpret the result in the VUDS+ sample as an indication of the global reversal of the SFR$-\delta_{\rm gal}$ relation at $z > 2$, a few considerations are necessary to test the veracity of this result. As mentioned in Sect. 2.5, the VUDS+ sample is nearly completely devoid of galaxies at the two extreme ends of the SFR spectrum: those that have ended their star-formation activity (i.e., quiescent) and those forming stars prodigiously (i.e., extremely obscured dusty star-forming galaxies). These galaxy populations are known to be associated with at least some overdensities at these redshifts (e.g., Kodama et al. 2007; Gobat et al. 2011; Casey et al. 2015; Wang et al. 2016; Smolčić et al. 2017a; Forrest et al. 2020; Zhou et al. 2020; Loiacono et al. 2021; Shen et al. 2021; Shi et al. 2021). To incorporate the potential effects of such galaxies in the SFR$-\delta_{\rm gal}$ relation, we began by estimating the number of each of the two galaxies populations that should exist in our VUDS+ sample were it truly representative of the underlying photometric sample.

Starting with the COSMOS2015 catalog, objects were selected in the photometric range $2 < z_{\rm phot} < 5$ and, as in our

[15] The term core can be a little deceptive here as such regions can still be quite large, e.g., $R_{\rm proj} = 0.5-1$ Mpc (Cucciati et al. 2018), values that rival $R_{\rm vir}$ values of massive clusters at $z \sim 1$ (e.g., Lemaux et al. 2012).

final spectral sample, limited to $\log(M_*/M_\odot) > 9$ and [3.6] < 25.3. The COSMOS2015 catalog is chosen because it is the deepest of our three photometric catalogs. The percentage of quiescent galaxies in this sample was estimated by counting the number of galaxies that populated the quiescent region of rest-frame $NUVrJ$ color–color as defined by Lemaux et al. (2014b):

$$\begin{aligned} &M_{NUV} - M_r > 3.45 && (M_r - M_J < 0.8) \\ &M_{NUV} - M_r > 2.8(M_r - M_J) + 1.21 && (M_r - M_J \geq 0.8). \end{aligned} \quad (1)$$

For dusty star-forming galaxies, we estimated their fractional contribution by counting the number of objects that had rest-frame $NUVrJ$ colors that indicate an excess extinction of $A_V \geq 1.5$ relative to the average COSMOS2015 object at these redshifts, which is characterized by median $NUV - r$ and $r - J$ colors of 1.06 and 0.33, respectively. More specifically:

$$\begin{aligned} &M_{NUV} - M_r > 2 \ \wedge \ M_{NUV} - M_r > \frac{3.7}{M_r - M_J + 0.3} \ \wedge \\ &M_r - M_J > 0.7 \ \wedge \ M_{NUV} - M_r \leq 3.45 \quad (M_r - M_J < 0.8) \\ &M_{NUV} - M_r \leq 2.8(M_r - M_J) + 1.21 \qquad (M_r - M_J \geq 0.8). \end{aligned} \quad (2)$$

Using the cuts defined in Eqs. (1) and (2), the fractional contribution of quiescent and dusty star-forming galaxies were found to be 0.8% and 4.2%, respectively.

While these are modest fractions in both cases, both populations lie at extreme values of SFR, so their contribution is necessary to quantify. In addition, the detection image used for the COSMOS2015 catalog was chosen to be a $z^{++}YJHK$ χ^2 image rather than the [3.6] image (see Laigle et al. 2016 for details). As a consequence, a small number of dusty, and therefore very red, highly star-forming galaxies at high redshift may be missing from the COSMOS2015 catalog even if they satisfy our adopted limiting magnitude in the [3.6] band. As such, their contribution may be underestimated here. We note, however, that that deep K-band observations are generally successful in detecting highly obscured dusty star forming galaxies at these redshifts (e.g., Romano et al. 2020; Zhou et al. 2020), as is the COSMOS2015 catalog in general (e.g., Gruppioni et al. 2020). Regardless, the results presented in this paper do not change meaningfully if we impose that the fractional contribution of such galaxies is increased by a factor of, for example, two, a number which roughly corresponds to the approximate incompleteness of the COSMOS2015 catalog for sources detected at far-infrared or radio wavelengths (Gruppioni et al. 2020; Zamorani, priv. comm.). Though we have no comparable estimate of the level of incompleteness of quiescent galaxies, as only a fraction of this population are bright in far-infrared/radio wavelengths, we find that our results are not meaningfully changed if the number of quiescent galaxies is doubled in the exercise described below.

Following the determination of the fractional contribution of underrepresented populations in our VUDS+ sample, a Monte-Carlo simulation was run in the following manner. For each of the 1000 iterations of the simulation, SFR and $\log(1+\delta_{\rm gal})$ values were recalculated for each of the galaxies in the VUDS+ sample by Gaussian sampling their associated uncertainties. To this, the appropriate number of quiescent and dusty star-forming galaxies were added, ~50 and ~300, respectively, at random overdensity values taken from the VUDS+ $\log(1 + \delta_{\rm gal})$ distribution. Each quiescent galaxy was assigned an SFR = 0. Each dusty star-forming galaxy was assigned a SFR statistically by sampling from a $\log(\mathrm{SFR}/M_\odot/\mathrm{yr})$ distribution with a mean of 3.25 and a $\sigma = 0.12$. Such values are appropriate for this galaxy population at these redshifts (e.g., Lemaux et al. 2014b; Smolčić et al. 2017a). For each of the 1000 iterations, the Spearman correlation coefficient was calculated as well as the significance of the rejection of the null hypothesis of no correlation. A weak ($\bar{\rho}_{\mathrm{SFR}-\delta_{\rm gal}} = 0.08$) but still highly significant (~8.5σ on median) positive correlation between SFR and $\log(1+\delta_{\rm gal})$ was found over all iterations, with no iterations returning a significance of $<6\sigma$.

As mentioned earlier, however, there are some hints that such galaxy populations are found to be associated with overdense environments at high redshift (e.g., Kubo et al. 2013; Wang et al. 2016; Smolčić et al. 2017a; Miller et al. 2018; Strazzullo et al. 2018; Shi et al. 2019, 2020; Hill et al. 2020). As such, we repeated this exercise by sampling only from $\log(1 + \delta_{\rm gal})$ values from those VUDS+ galaxies found in non-field environments, in other words, either the Intermediate or Peak regions as defined earlier in this section. Since dusty star-forming galaxies outnumber quiescent galaxies by a factor of approximately six in this simulation, forcing these populations to reside in overdense regions only serves to increase both the strength and significance of the observed positive correlation between SFR and $\delta_{\rm gal}$. As these tests account for the full range of the effect of measurement errors, and, in conjunction with those tests given in Sect. 3.3, account for the effect of galaxy populations missing in our data, we conclude the reversal of the SFR$-\delta_{\rm gal}$ relation observed in the VUDS+ sample is a real feature of the galaxy population in the early universe.

3.2. Stellar mass and redshift effects on the SFR$-\delta_{\rm gal}$ relation

Plotted in the right panel of Fig. 5 is the equivalent relation between M_* and $\log(1 + \delta_{\rm gal})$. As in its SFR equivalent, a steady, nearly monotonic increase in M_* and $\log(1 + \delta_{\rm gal})$ is observed at about the same level (~0.3 dex) as that of the SFR over the same dynamic range in local environments. The Spearman's correlation coefficient is essentially equivalent to that calculated for SFR, $\rho_{M_*-\delta_{\rm gal}} = 0.15$, as is the significance of the positive correlation (~12σ). Because the star-forming properties of galaxies relate in a complex way to stellar mass, as well as redshift and environment (e.g., Peng et al. 2010; Wuyts et al. 2011; Tasca et al. 2015; Tomczak et al. 2016, 2019; Lemaux et al. 2019), the level of concordance of the $M_*-\delta_{\rm gal}$ and SFR$-\delta_{\rm gal}$ relations seen in the VUDS+ sample suggests that stellar mass effects may be primarily responsible for driving the observed SFR$-\delta_{\rm gal}$ relation. In other words, higher stellar mass star-forming galaxies are preferentially situated in high-density environments in the VUDS+ sample. That these higher stellar mass star-forming galaxies, whether through an increased gas supply or a higher star-forming efficiency (e.g., Schinnerer et al. 2016; Scoville et al. 2016, 2017; Wang et al. 2018), have, on average, higher SFR values (e.g., Rodighiero et al. 2014; Tasca et al. 2015; Tomczak et al. 2016), could explain the observed SFR$-\delta_{\rm gal}$ relation. Such an explanation is still wanting in that the increased presence of higher M_* in higher-density environments has to be accounted for by some process acting at earlier times, but it at least could potentially explain the increase in SFR with increasing $\log(1 + \delta_{\rm gal})$.

In the left panel of Fig. 6 is plotted SFR vs. $\log(1 + \delta_{\rm gal})$ in three different bins of stellar mass defined as low, mid, and high M_* by the stellar mass ranges indicated in the bottom right of that plot. In all three cases a significant positive correlation, as quantified by a Spearman's test, is observed, with $\rho_{\mathrm{SFR}-\delta_{\rm gal}}$ ranging from 0.08 to 0.09 depending on the bin and a $>3.5\sigma$ rejection of the null hypothesis in each bin. This trend is relatively weak for the two lowest stellar mass bins, while slightly

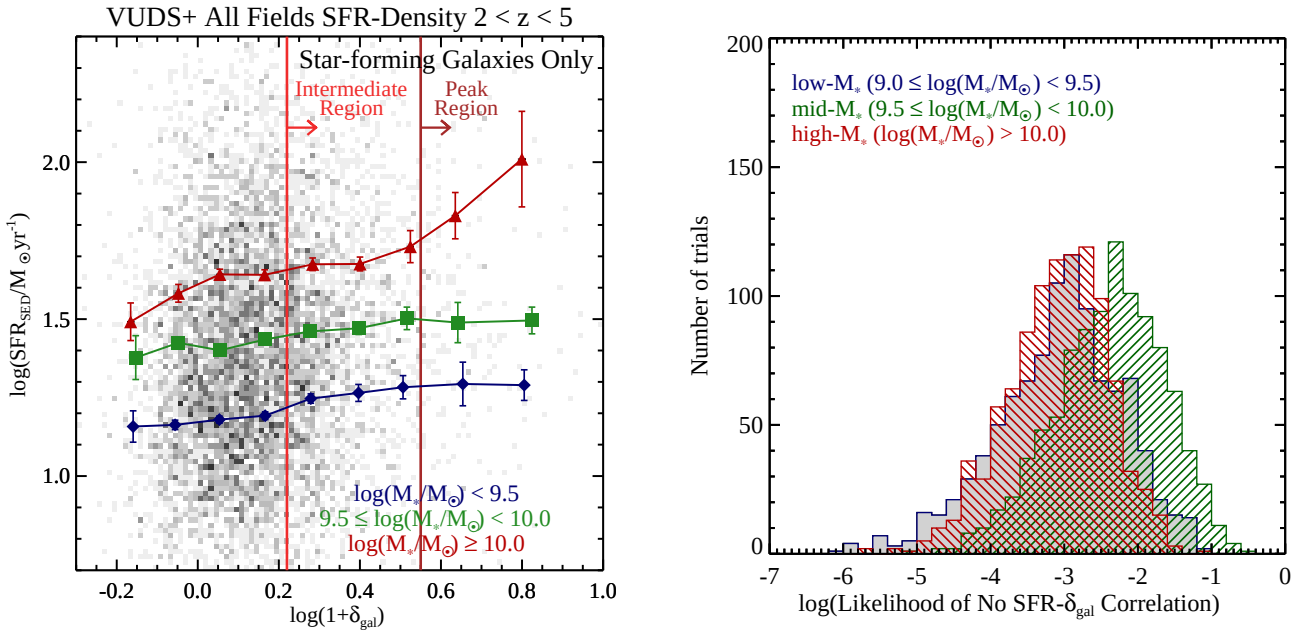

Fig. 6. The SFR−density relation in the VUDS+ sample as a function of stellar mass. *Left*: as in the left panel of Fig. 5, the SFR–δ_{gal} relation for our final VUDS+ sample, but now with galaxies broken up into three approximately equally-sized samples binned in stellar mass using the limits indicated at the bottom right of the panel. The points and their associated uncertainties have the same meaning as in Fig. 5. The solid vertical lines and their meanings are the same as in Fig. 5. A weak but significant positive correlation between SFR and $\log(1+\delta_{gal})$ is seen in the two lower mass bins. A stronger and equally significant positive correlation is seen for the highest stellar mass galaxies and is especially apparent in the Peak Region. *Right*: distribution of the logarithmic value of the likelihood of no correlation between SFR and $\log(1+\delta_{gal})$ of our final spectral sample for the three different stellar mass bins used in our analysis for the full redshift range $2 \le z \le 5$. This distribution is calculated from 1000 Monte Carlo realization in which we perturb each SFR and $\log(1+\delta_{gal})$ value by their associated errors. These histograms do not meaningfully change if we additionally include dusty star-forming galaxies with high rates of SFR and galaxies with no active star formation, both of which are completely missed in our sample, at proportions appropriate for their number density at $2 \le z \le 5$ in our Monte Carlo simulations. For reference, a log(likelihood)<−2.5 corresponds to a positive correlation between the two parameters estimated at $\ge 3\sigma$ confidence level.

stronger for the galaxies in our sample that are the most massive in their stellar content. We note that these statements hold if we instead restrict the highest stellar mass bin to the stellar mass range $10 \le \log(M_*/M_\odot) \le 10.5$ to remove any residual stellar mass-driven trends due to the wideness of that bin. As was done in Sect. 3.1, the reliability of these trends were tested by running a Monte-Carlo simulation for each of the three samples. Because the stellar mass distribution of quiescent and dusty star-forming galaxies is not known, in this simulation we ignore their fractional contribution and only vary the SFR and $\log(1+\delta_{gal})$ of observed VUDS+ galaxies based on their formal uncertainties. However, this analysis is not meaningfully changed if we include their contribution equally across all M_* bins, or, since both galaxy populations are almost certainly some of the most massive at these redshifts (see, e.g., Casey et al. 2014; Tomczak et al. 2014 and references therein), exclusively limit them to the higher-M_* bins. Plotted in the right panel of Fig. 6 is the distribution of the probability of the null hypothesis that SFR and $\log(1+\delta_{gal})$ are uncorrelated being correct for each of the three stellar mass samples across the 1000 Monte-Carlo iterations. For the vast majority of the iterations (∼80−90%) for the low- and high-M_* bins, a significant ($>3\sigma$, log(Likelihood) < -2.5) positive correlation between SFR and $\log(1+\delta_{gal})$ is observed. For the mid-M_* bin, the trend is weaker, though ∼50% of the iterations still return a significantly positive SFR−δ_{gal} correlation. It appears that even at fixed stellar mass, environmental effects serve to drive an increase in star formation in higher-density environments. Additionally, whatever this effect, it appears to be most effective on high-M_* galaxies, as such galaxies increase their SFR by more than a factor of three from the lowest to the highest densities.

In order to investigate the possible redshift evolution of the SFR−δ_{gal} relation, in the two panels of Fig. 7 we show the same plot as was shown in the left panel of Fig. 5 but now in two redshift bins. The lower-z bin is defined as $2 \le z \le 2.7$ and the higher-z bin as $2.7 < z \le 5$. These redshift ranges cut the sample approximately in half, allowing each bin to have considerable statistical power. Immediate differences can be seen between the two samples. In the lower-z bin, while the median SFR is seen to gently increase with increasing $\log(1+\delta_{gal})$ in the Field and Intermediate regions, a turnover is observed in the Peak region that is strong enough to decrease the SFR in the highest-$\log(1+\delta_{gal})$ bin to a value that is statistically indistinguishable (i.e., at a difference of $<1\sigma$) with that of the lowest-$\log(1+\delta_{gal})$ bin. Conversely, the increase in SFR with $\log(1+\delta_{gal})$ persists through the Peak region in the higher-z bin. While the correlation coefficient is not appreciably different between the two redshift bins ($\rho_{SFR-\delta_{gal}}$=0.13 and 0.14 in the lower- and higher-z bins, respectively), the differences are significant when considering only the Intermediate and Peak regions. For galaxies with $\log(1+\delta_{gal}) > 0.22$, no significant SFR−$\delta_{gal}$ relation exists at $2.0 \le z \le 2.7$ ($\rho_{SFR-\delta_{gal}} = 0.04$ with a rejection of the null hypothesis of no correlation at $<2\sigma$). While a flat relation is still considerably different from the negative correlation observed at lower z (i.e., $z < 2$), galaxies in the higher-z bin exhibit a dramatic and significant increase in their SFR with increasing $\log(1+\delta_{gal})$ in the Intermediate and Peak regions ($\rho_{SFR-\delta_{gal}} = 0.17$, $\sim 5\sigma$). These results combined with the previous results binned by stellar mass imply

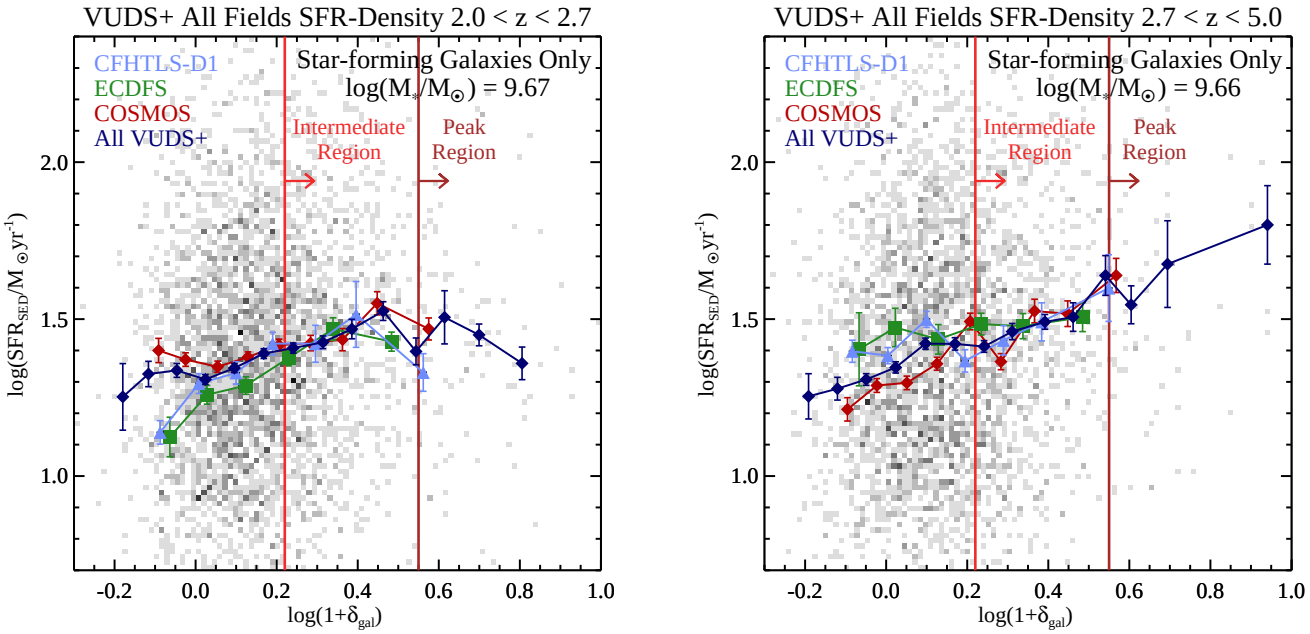

Fig. 7. The redshift dependence of the SFR$-\delta_{\rm gal}$ relation in the VUDS+ sample. The *two panels* are identical to the *left panel* of Fig. 5 except now the VUDS+ sample is broken up into two redshift bins with approximately equal numbers of galaxies. The meaning of the points and their associated uncertainties are identical to those in Fig. 5 as are the meanings of the vertical lines. As in Fig. 5, the SFR$-\delta_{\rm gal}$ for all three VUDS+ fields are shown along with the combined sample. *Left panel*: SFR$-\delta_{\rm gal}$ relation for the lower-redshift sample ($2.0 \leq z \leq 2.7$) and the *right panel* shows the relation for the higher-redshift sample ($2.7 < z \leq 5.0$). The average stellar mass of each sample is given in the top-right portion of each panel and is effectively identical between the two samples. While a significant positive correlation between SFR$-\delta_{\rm gal}$ exists in the lower-redshift sample, this correlation disappears when considering only galaxies in the Intermediate and Peak regions. In contrast, in the higher-redshift bin, the significant positive correlation is seen at all environments and increases in strength in the densest regions.

that it is primarily higher stellar mass, higher-redshift galaxies that are driving the global reversal of the SFR$-\delta_{\rm gal}$ at these redshifts.

Some caution in extrapolating these results is necessary, however. While galaxies in the Intermediate region of the higher-z bin are drawn from a variety of different structures, a considerable fraction of the galaxies in the Peak region are members of PCl J1001+0220 at $z \sim 4.57$ in the COSMOS field. Even so, this trend does persist at a similar significance and strength even after excising the members of PCl J1001+0220. Additionally, it is clear from the right panel of Fig. 7 that this trend is also present in the CFHTLS-D1 and ECDFS fields, though at a less significant level (~2–3σ per field, >3σ for the two fields combined). However, the number of galaxies in the peak region across all fields after excising the PCl J1001+0220 members is sufficiently small (~60 galaxies) to make sample variance a concern. Further data, both in PCl J1001+0220, and in structures at similar redshifts across the VUDS fields, will be necessary to see if such trends are general or isolated to a particular system or small set of proto-structures.

Finally, we perform two tests in an attempt to further separate out the effects of stellar mass and redshift from those of environment in driving the SFR$-\delta_{\rm gal}$ relation. The first of these tests is a Spearman's partial rank correlation test, which is a formalism designed to estimate the strength and significance of the correlation between two variables after removing the contribution of other variables to the observed correlation. In this case, we are interested in computing the correlation between SFR and $\log(1+\delta_{\rm gal})$ after removing the effects of M_* and z. The calculation that follows adopts the Spearman's partial rank correlation methodology described in Macklin (1982), in which it was shown that this test is efficient for the purpose of separating out the effect of different variables in inducing observed correlations. The Spearman's partial rank coefficient, $\rho_{\rm p}$, for SFR and $\log(1+\delta_{\rm gal})$ was calculated to be $\rho_{\rm p,SFR-\delta_{\rm gal}} = 0.07$ with a significance of ~6σ. In other words, while the strength of the SFR–$\delta_{\rm gal}$ correlation has depreciated by approximately 50% after taking into account the correlation between both M_* and z and SFR, though mostly the former, the correlation between SFR and $\delta_{\rm gal}$ still remains extremely significant. Incidentally, the same is true if the sample is confined to only those galaxies in the COSMOS field, though at a significance of ~4σ.

The result of the second test is shown in Fig. 8. In this test, galaxies are divided into ten equally-populated bins[16] in $\log(1+\delta_{\rm gal})$ and forced to have the same median stellar mass and redshift across all bins to within the uncertainties of the median values in each bin. For each bin, galaxies at the extreme low end of the stellar mass distribution, but still always with $\log(M_*/M_\odot) > 9$, and the extreme high end of the redshift distribution were removed until the median values in each bin converged, within their associated uncertainties, to the values shown in the top right of Fig. 8. The median value of the SFR for each $\log(1+\delta_{\rm gal})$ is overplotted against the backdrop of the individual measurements of the ~5700 galaxies that remain in the M_*/z-matched sample. Also shown in the top right of Fig. 8 is $\rho_{\rm SFR-\delta_{\rm gal}}$ for the M_*/z-matched sample and the probability of the null hypothesis of no correlation between SFR and $\log(1+\delta_{\rm gal})$. It appears that regardless of how the data are analyzed, there is a weak but highly significant positive correlation between

[16] The bins representing the lower and upper 10% of the $\log(1+\delta_{\rm gal})$ distribution were cut in half for illustrative purposes. This choice does not affect our analysis, which is performed on the individual galaxies in the clipped sample.

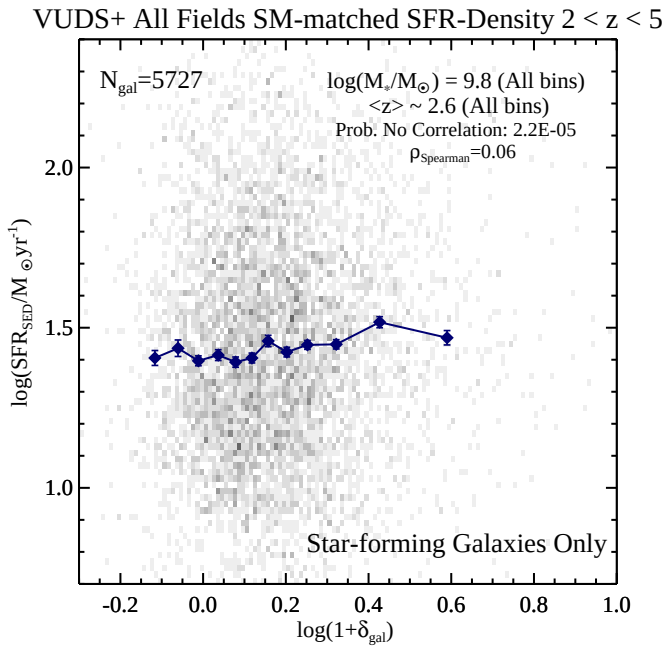

Fig. 8. Relationship between SFR and $\log(1+\delta_{\rm gal})$ for a stellar-mass- and redshift-matched sample of galaxies. Each bin in $\log(1+\delta_{\rm gal})$ originally contained 10% of the final VUDS+ sample. Galaxies in each decile were clipped in order to have the same median redshift and stellar mass within the uncertainties with every other decile. The bins in the lower and upper decile of the $\log(1+\delta_{\rm gal})$ distribution were cut in half for illustrative purposes. The approximate median stellar mass and redshift of all bins is indicated in the top right and the number of galaxies remaining in the sample indicated in the top left. The data points and their associated uncertainties were calculated in the same way as Fig. 5. In the top right of the plot the Spearman's correlation coefficient for this sample and the likelihood of no correlation are shown. Despite normalizing by stellar mass and redshift, a weak but significant positive SFR$-\delta_{\rm gal}$ trend is observed.

SFR$-\delta_{\rm gal}$ and that at least some part of that trend is driven by environmental effects.

3.3. Effects of lack of spectral representativeness on the SFR$-\delta_{\rm gal}$ relation

In Sect. 2.5 we discussed the lack of spectral representativeness of the VUDS+ sample. In particular, we noted that, at a given M_*, objects in the parent photometric sample at bluer colors in the range $2 < z_{\rm phot} < 5$ generally appeared to have a higher percentage of spectroscopic redshifts. This trend is shown again in the left panel of Fig. 9, where we now plot the spectral fraction of objects in the NIR-selected photometric parent sample in coarser bins of 0.5 and 0.25 in $M_{NUV} - M_r$ color and M_*, respectively. In each two-dimensional bin, the number of galaxies with spectral redshifts within the redshift range considered in this paper ($2 \leq z \leq 5$) are given as the top number. The number of objects that have $z_{\rm phot}$ values within the redshift range considered here that either do not have a spectral redshift or have a spectral redshift within our adopted redshift range is given as the bottom number in each bin. The color bar indicates the $z_{\rm spec}$ fraction in each bin.

It is again apparent from inspection of the left panel of Fig. 9 that galaxies in the spectral sample preferentially have a secure spectral redshift at the bluest colors at a given stellar mass, as $z_{\rm spec}$ fractions appear at ~25–75% for the bluest colors and $\lesssim$5% for the reddest colors across nearly the entire stellar mass range plotted. As mentioned in Sect. 2.5, galaxies on the red extreme of the color distribution at a given stellar mass are subdominant, both in the $z_{\rm phot}$ sample and, in terms of absolute numbers, in the spectral sample (see Fig. 4). Therefore, the main channel for them to disrupt a general analysis is if the average SFRs are considerably higher than their counterparts at bluer colors[17]. If this were the case, it would perhaps make our results more sensitive to small sample statistics and the sampling of such galaxies in each environment.

In the right panel of Fig. 9 the average SED-derived SFR is shown in two-dimensional bins of color and stellar mass for the same observed-frame NIR-limited sample. It is immediately clear in this figure that objects appearing at redder colors generally show depreciated levels of star formation at fixed stellar mass relative to their bluer counterparts. Further, the decrease in SFR is a slowly varying, smooth function of color and stellar mass for the populations plotted here. Because of the lack of stark change in the average SFR for the bulk of this sample, the relative scarcity of redder galaxies at a given stellar mass, and the fact that we are preferentially sampling galaxies at the high end of the SFR distribution at a given stellar mass (with the notable exception of extremely dusty starbursts), it is unlikely that the bias seen in the left panel of Fig. 9 meaningfully affects the main conclusions presented in this paper.

Despite the high likelihood of our results being invariant to this sampling effect, we formally tested the possible effect of this selection bias on our results in the following manner. We begun by looking at the spectral representativeness in each bin of color and stellar mass plotted in the left panel of Fig. 9 by means of one-dimensional KS tests. For each bin in color and stellar mass, a KS test was run on the distribution of the $z_{\rm phot}$ objects and $z_{\rm spec}$ galaxies in that bin. For nearly all (80%) of the bins in stellar mass and color running $-0.5 \leq M_{NUV} - M_r \leq 4$ and $9 \leq \log(M_*/M_\odot) \leq 11.5$ for bins that had sufficient numbers of both $z_{\rm spec}$ and $z_{\rm phot}$ objects, $N > 3$ and $N > 20$, respectively, the KS test did not return a significant rejection of the null hypothesis ($>3\sigma$) that the two distributions were drawn from the same sample. We conclude from this exercise that the final spectral sample is broadly representative of the non-dusty star-forming galaxy population at these redshifts in each individual color-M_* bin. This representativeness allows us to leverage the spectral sample in each individual color-M_* bin to proxy as the underlying photometric sample.

Following this, we attempted to homogenize the $z_{\rm spec}$ fraction using a Monte Carlo approach. We begun by identifying all color-M_* bins in the left panel of Fig. 9 that we consider well-sampled spectroscopically. For the purposes of this exercise, we defined this term as any bin whose $z_{\rm spec}$ fraction is $\geq$3% and the number of galaxies with a secure $z_{\rm spec}$ exceeds three. These cuts included the majority (70.0%) of all photometric objects within this redshift range and the results of this exercise do not meaningfully change if we slightly adjusted these limits. We then set a fiducial $z_{\rm spec}$ fraction that we will homogenize each color-M_* bin to for all Monte Carlo iterations. If the $z_{\rm spec}$ fraction exceeded this fiducial value for a given bin, for each Monte Carlo realization, we randomly sampled the SFR and $\log(1+\delta_{\rm gal})$ values from the available $z_{\rm spec}$ galaxies in that bin only enough times to reduce the $z_{\rm spec}$ fraction to the fiducial value. If the $z_{\rm spec}$

[17] As a reminder, we are considering here only star-forming galaxies with low to moderate dust contents. Extremely dusty star-forming galaxies and sub-millimeter populations are considered in Sect. 3.1.

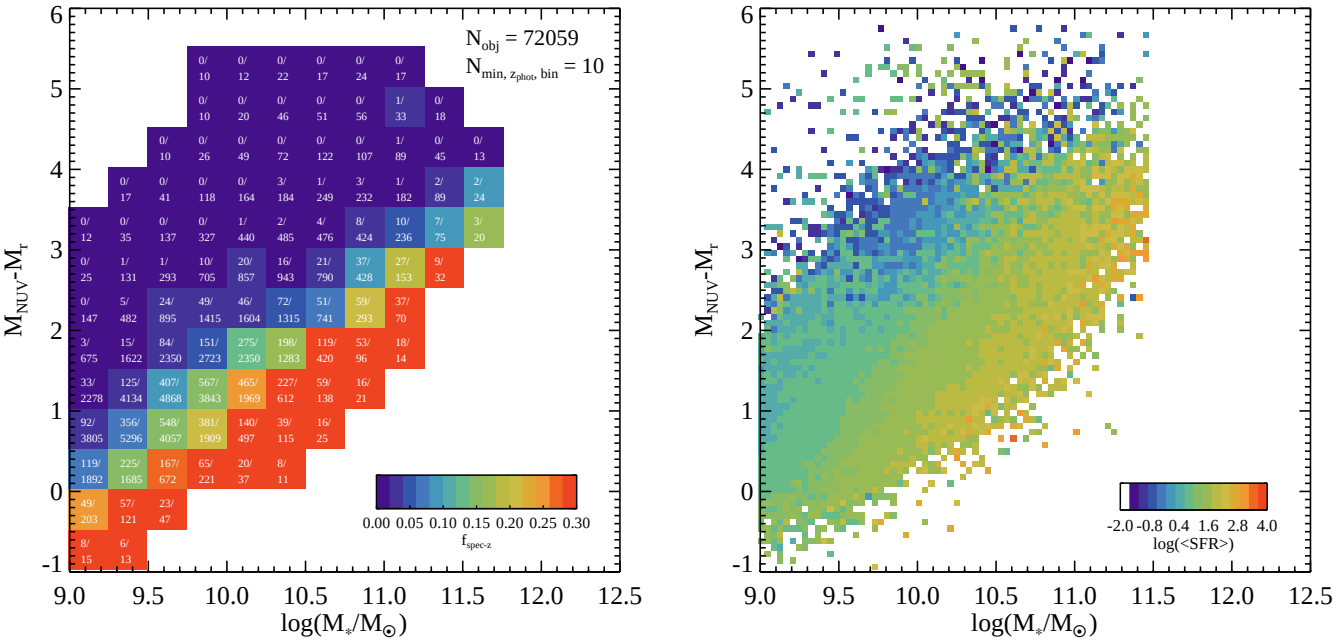

Fig. 9. Color, stellar mass, and SFR properties of the VUDS+ spectroscopic and parent photometric sample. *Left*: rest-frame color–stellar mass diagram of an observed-frame NIR-selected sample of $z_{\rm phot}$ and $z_{\rm spec}$ objects in across the three VUDS fields. The fraction of $z_{\rm phot}$ objects with a secure spectral redshift in each color/stellar mass bin is indicated by the color bar. In each color/stellar mass bin the number of $z_{\rm spec}$ and $z_{\rm phot}$ objects are given by the upper and lower number in each box, respectively. Only those bins that contained ten or more $z_{\rm phot}$ objects are plotted. This plot is nearly identical to the right panel of Fig. 4, but here the bins are coarser to reflect the size used to perform the weighted Monte Carlo SFR–$\delta_{\rm gal}$ analysis presented in this section. *Right*: color–stellar mass diagram of the $z_{\rm phot}$ sample plotted in the left panel with the color bar now corresponding to the average SED-fit SFR of all objects in that bin. No color or stellar mass limits are imposed on the galaxies plotted here, and two-dimensional bins are now plotted if they contain at least one object. The average SFR is seen to vary smoothly as a function of color and stellar mass over the range plotted. While the clear preference of the VUDS+ spectral sampling toward bluer galaxies at fixed M_* appears to potentially bias the spectral sample to higher SFRs, from the analysis presented in this section we conclude that this potential bias does not drive the significant positive correlation between SFR and $\delta_{\rm gal}$ seen in the full VUDS+ sample.

fraction was below this fiducial value for a given bin, in addition to keeping all $z_{\rm spec}$ galaxies in that bin, we again randomly sampled all $z_{\rm spec}$ galaxies in this bin a sufficient number of times to raise the $z_{\rm spec}$ fraction to the fiducial value. At the end of this process, for each bin that is well-sampled spectroscopically, the $z_{\rm spec}$ fraction is homogenized to the fiducial value and a unique set of SFR and $\log(1+\delta_{\rm gal})$ values were generated for that iteration. A fiducial $z_{\rm spec}$ fraction of 0.2 was chosen here as an intermediate value to all those shown in the left panel of Fig. 9, though the results of this exercise do not change meaningfully if this fraction is slightly varied.

At the end of each Monte Carlo iteration, we calculated the Spearman ρ and significance of the rejection of the null hypothesis that the two parameters are uncorrelated. Over 1000 Monte Carlo iterations we found a rejection of the null hypothesis at $>3\sigma$ for all iterations, with a median significance of 6.9σ and a median $\rho_{\rm SFR-\delta_{gal}} = 0.07$. While the strength of the correlation is slightly lower than that of the full spectral sample (see Sect. 3.1), this is expected given that the random sampling of the SFR and $\log(1+\delta_{\rm gal})$ values in the Monte Carlo process necessarily dilutes the true signal when averaging over a large number of realizations. Though we did not strictly impose the stellar mass and color limits used in this exercise (i.e., $-0.5 \leq M_{NUV} - M_r \leq 4$ and $9 \leq \log(M_*/M_\odot) \leq 11.5$) to define the final VUDS+ spectral sample, these galaxies make a small contribution (<10%) to the overall sample. Additionally, the main conclusions of this study do not change meaningfully if we instead limit the final VUDS+ sample to the >6000 galaxies with $\log(M_*/M_\odot) \geq 9$ and $M_{NUV} - M_r \geq -1$.

3.4. Comparison of the observed SFR–$\delta_{\rm gal}$ relation to other works

While a rigorous comparison of the observed VUDS+ SFR–$\delta_{\rm gal}$ relations derived in Sects. 3.1 and 3.2 and those predicted in simulations is deferred to future work, we take here a few points of comparison. The first point of comparison relies on Elbaz et al. (2007), who used light cones generated by Kitzbichler & White (2007) to estimate the SFR–$\delta_{\rm gal}$ predicted at different redshifts from the Millennium simulation (Springel et al. 2005) as interpreted through the lens of the semi-analytic model of Croton et al. (2006). This prediction showed an increase of ~0.25 dex at both $z \sim 2$ and $z \sim 3$ from the most rarefied to densest environments measured in the simulation[18]. While the SFRs as measured in the VUDS+ sample are offset higher from these predictions by ~0.1–0.2 dex across all environments, likely due to some combination of differing redshift ranges, ranges of SFRs and M_* probed, and differences in the assumed properties of the models used to infer physical properties, the magnitude of the increase in the average SFR across the full density range measured in the VUDS+ sample is essentially identical to that predicted in the Millennium simulation. Such behavior was also predicted in the N-body simulations of De Lucia et al. (2004).

[18] These light cones use the full Millennium simulation, which contains many structures massive enough to be considered as proto-groups or proto-clusters (see, e.g., Chiang et al. 2017; Araya-Araya et al. 2021), and thus span a similar dynamic range in environments as the VUDS+ sample. The same is true for the IllustrisTNG simulations discussed later in this section (see, e.g., Bose et al. 2019).

Using semi-analytic prescriptions to estimate SFRs of cluster and field galaxies, De Lucia et al. (2004) predicted the reversal of the SFR$-\delta_{\rm gal}$ relation at $z \sim 2.5$, with the normalized average rate of star production of cluster galaxy outpacing field galaxies by ∼0.2 dex in the redshift range corresponding to the higher-redshift portion of our sample ($2.7 \leq z \leq 5$). More recently, similar behavior was also seen in Hwang et al. (2019), where the predictions of the SFR$-\delta_{\rm gal}$ from the TNG300 run of the IllustrisTNG project (Nelson et al. 2019) were investigated. While this investigation is only performed over the redshift range $0 \leq z \leq 2$, a range that just barely intersects with that of the VUDS+ sample, at $z = 2$, a ∼0.3 dex increase in the average SFR is seen from the lowest to highest-density environments for a sample of galaxies with comparable M_* values to those in the VUDS+ sample. Again, while the VUDS+ galaxies appear to be biased to slightly higher SFRs across all redshifts, the magnitude of the increase in the average SFR across the full dynamic range of environments in the VUDS+ sample across the full redshift range is essentially identical to that observed in the TNG300 simulations. However, when considering only the lower-redshift ($2.0 \leq z \leq 2.7$) VUDS+ sample, the sample that is most relevant for this comparison, a more modest increase is seen in our data of ∼0.1 dex. Such an increase is in moderate tension with the results presented in Hwang et al. (2019), though the disparate environmental metrics in the VUDS+ and Hwang et al. (2019) samples preclude a direct comparison. Further work with these simulations using a common environmental metric and spanning the full VUDS+ redshift range would help to illuminate if any real tension exists.

Our results are also qualitatively consistent with predictions of updated semi-analytic models applied to the Millennium simulation (Chiang et al. 2017), in which the volume-averaged star-formation activity within proto-cluster environments, in other words, those regions corresponding to our Intermediate and Peak regions, is predicted to well outpace that of the field at $z > 2$. Other simulations that suggest a strong reversal at later epochs ($z \sim 1$, Tonnesen & Cen 2014) are qualitatively inconsistent with our results, especially the flattening in the SFR$-\delta_{\rm gal}$ observed in the lower-redshift portion of our data (see Sect. 3.2). Such a reversal globally persisting to $z \sim 1$ is also ruled out by the observed anticorrelation between SFR$-\delta_{\rm gal}$ and the fractional increase of quiescent galaxies in dense environments seen in large surveys of $z \sim 1$ clusters and groups (e.g., Lemaux et al. 2019; Tomczak et al. 2019). Future work involving more comprehensive comparisons to these and other cosmological simulations will be extremely helpful to inform the mechanisms that drive this reversal at $z \gtrsim 2$.

From an observational perspective, of note is the stark contrast of the observed SFR$-\delta_{\rm gal}$ relation in the VUDS+ sample to that observed in Chartab et al. (2020) the five CANDELS fields[19]. In that study, a clear negative correlation was observed between SFR and $\delta_{\rm gal}$ across the entire redshift range running from $0.4 \leq z < 3.5$ over a similar range of local overdensities as was probed in our study. Though nearly identical methodologies were used to estimate SFRs in the two studies, the differences in the size of the sample, the metric of environment, the spectroscopic selection method, and the inclusion of photometrically selected galaxies in their sample make the genesis for the different SFR$-\delta_{\rm gal}$ behavior difficult to isolate. It is possible that cosmic variance effects could explain at least some of the observed difference, as the combined areal size of the CANDELS fields is approximately an order of magnitude smaller than area probed in our study. In order to test the likelihood that cosmic variance is the primary driver of the difference in behavior observed in the two samples, we broke up the VUDS+ sample into 100 different nonunique subsamples that probe the same volume as the sample in Chartab et al. (2020). In all 100 samples we observed a significant ($>3\sigma$) positive correlation between SFR and $\delta_{\rm gal}$, with an average $\rho_{\rm SFR-\delta_{gal}}$ of 0.15. Thus, it is likely that cosmic variance is not the primary source of the observed tension. The consideration that the strength of the observed SFR$-\delta_{\rm gal}$ correlation is strongest in the higher-redshift portion of our sample, a redshift range largely unprobed by Chartab et al. (2020), does serve to somewhat alleviate this tension.

[19] Two of the CANDELS fields, GOODS-S and COSMOS, are covered in the VUDS+ sample.

3.5. *Interpreting the reversal of the* SFR – $\delta_{\rm gal}$ *relation*

We have shown in the previous sections that the reversal of the SFR$-\delta_{\rm gal}$ in the redshift range $2 < z < 5$ for VUDS+ galaxies is real and that these results are very likely applicable to the general population of $\log(M_*/M_\odot) > 9$ galaxies at these redshifts. Despite the complicated relationship demonstrated between the average SFR of VUDS+ galaxies and stellar mass, redshift, and galaxy environment, we found increased star-formation activity in dense environments even after stellar mass and redshift effects were taken into account. Such definitive results were possible only by the immense spectroscopic data set compiled here as well as the supporting ancillary data and methodologies that allowed for accurate and precise estimates of each of these parameters. Given the weakness of the trends observed in the data and their large dispersion, a smaller sample size of ∼1000 galaxies with spectroscopic redshifts, if sampled representatively from the galaxy sample observed here, would not yield sufficiently confident rejections ($>3\sigma$) of the null hypothesis of lack of correlation for many of the interdependences seen here.

In this section we attempt to leverage these interdependences to speculate on the possible mechanisms that drive the measured decrease in the positive correlation between SFR$-\delta_{\rm gal}$ from the higher- to the lower-redshift bin. Several mechanisms present themselves as possible explanations for the observed behavior. For this discussion we will assume that the overdense structures probed and their constituent galaxies in the higher-redshift bins are possible progenitors of those observed in the lower-redshift bin. This may or may not be a valid assumption and will eventually need to be verified by the use of simulations (e.g., Ascaso et al. 2014) and semiempirical models (e.g., Tomczak et al. 2017). Given the large number of galaxies in the VUDS+ sample and the large number of structures probed, it is likely there is at least some level of truth to this assumption. Additionally, we again note that a considerable fraction (∼50%) of the high-$\delta_{\rm gal}$, high-M_* galaxies in the higher-redshift bin belong to the $z \sim 4.57$ PCl J1001+0220 proto-cluster, and, thus, sample variance effects may be considerable. Future observations from the C3VO survey with Keck/DEIMOS and Keck/MOSFIRE of the most massive proto-clusters detected in VUDS across the full redshift range studied here will be crucial to determining the level of this effect. Additional future wide-field observations from instruments such as the Subaru Prime Focus Spectrograph (PFS; Sugai et al. 2012), the Multi Object Optical and Near-infrared Spectrograph (MOONS; Cirasuolo et al. 2014) on the VLT, or dedicated observations of specific proto-clusters with the *James Webb* Space Telescope (JWST, Gardner et al. 2006) will mitigate sample variance effects and immensely aid in the calibration of various physical parameters.

Putting aside the above concerns, it appears that high-M_* galaxies in the densest environments in the higher-redshift bin are primarily driving the reversal of the SFR$-\delta_{\rm gal}$ relation. This is in stark contrast to the demographics of higher-M_* group and cluster galaxies in the low- and intermediate-redshift universe (i.e., $0 \leq z \leq 1.5$) where such galaxies broadly exhibit higher quiescent fractions and have average SFRs that are lower than their lower-M_* counterparts (see, e.g., Lemaux et al. 2019; Tomczak et al. 2019 and references therein). This dramatic change over the course of several Gyr is likely the result of multiple processes present in high-density environments that serve to both enhance star-formation activity at higher redshift and quench it at lower redshifts. In what follows, we explore the possible effect of these processes and review potential constraints on these processes from our own data as well as various studies from the literature.

3.5.1. Gas fraction and the SFR$-\delta_{\rm gal}$ relation

It has been well established by observations of large samples of galaxies, primarily with the Atacama Large Millimeter/submillimeter Array (ALMA) and the Plateau de Bure millimetre Interferometer (PdBI), that the fraction of gas mass to total baryonic mass ($\mu_{\rm gas}$) is a strong function of redshift, with galaxies exhibiting lower $\mu_{\rm gas}$ values at fixed stellar mass with decreasing redshift (see, e.g., Genzel et al. 2015; Schinnerer et al. 2016; Scoville et al. 2016, 2017). Adopting the formalism of Scoville et al. (2017), $\mu_{\rm gas}$ is predicted to drop by ∼10% in between the median redshift of our higher- and lower-redshift bins, with average rates of cosmological accretion (Dekel et al. 2009a,b) decreasing by more than a factor of two. By the time the SFR$-\delta_{\rm gal}$ relation is firmly seen as an anticorrelation. At $z \sim 1$, gas fractions have decreased, on average, by more than 20% at fixed stellar mass and expected gas accretion rates have declined by more than an order of magnitude relative to those at the median redshift of our higher-redshift sample. At fixed star-formation efficiency, such a decrease in gas mass will lead to an overall decrease in star formation across all environments.

However, it is reasonable to assume that environment would modulate both the accretion rates and gas fraction of galaxies in varying ways across different redshifts, potentially inducing excess accretion at some redshifts and stifling or ceasing accretion at other redshifts. While such evidence is sparse due to the lack of observations of consistent samples of galaxies residing in average- and high-density environments at all redshifts, there have been a few hints from ALMA observations of the possible effect of environment at different redshifts.

At the highest redshifts probed by our sample, such observations are still extremely limited. Recently, the ALMA Large Program to Investigate C^+ at Early times (ALPINE; Le Fèvre et al. 2020; Faisst et al. 2020; Béthermin et al. 2020) survey, while primarily designed as a field survey, has begun to probe high-density environments at $4 < z < 5$. In ALPINE, several galaxies in and around the PCl J1001+0220 proto-cluster in the COSMOS field were observed (see, e.g., Jones et al. 2020; Ginolfi et al. 2020a). In these observations, massive, diffuse gas envelopes were observed to be associated with several ongoing merging events within the greater proto-cluster environment. If the ambient medium has not been sufficiently heated, likely a fair assumption at these redshifts (e.g., Overzier 2016; Shimakawa et al. 2018b), some of this diffuse gas will likely be (re-)captured by the remnant galaxy. If most of this gas is retained, the resultant $\mu_{\rm gas}$ values would likely approach those observed in starburst galaxies (e.g., Scoville et al. 2016; Tacconi et al. 2018 though see also Silverman et al. 2018), which could result in the fueling of virulent star-formation activity (see, e.g., the discussion in Sect. 4.2 of Aoyama et al. 2022 and references therein). There also appears evidence of cold, diffuse gas in several proto-clusters in our VUDS+ sample (e.g., Cucciati et al. 2014; Newman et al. 2020) that may accrete on to galaxies as they coalesce into the proto-cluster environment (see, e.g., Shimakawa et al. 2017, 2018b for possible evidence of such a phenomenon). Such a process would naturally be more effective in higher stellar mass galaxies due to their larger potential well. By contrast, in a study of the core of the exceptional SPT2349-56 proto-cluster at $z \sim 4.3$, Hill et al. (2022) found smaller $\mu_{\rm gas}$ and depletion timescales for proto-cluster members than those of comparable field galaxies. Though many of these galaxies were extremely massive, with approximately half of the sample exhibiting stellar masses of $\log(M_*/M_\odot) > 11$, well in excess of most of the galaxies in the VUDS+ sample, these results suggest considerable variation across structures and different galaxy populations even at these early epochs.

At redshifts that correspond to the lower-redshift portion of our sample, $z \sim 2$–2.5, the gas fraction at fixed stellar mass appears to be somewhat anticorrelated with environment, with lower $\mu_{\rm gas}$ measured for at least some fraction of galaxies situated in denser environments (e.g., Coogan et al. 2018; Wang et al. 2018; Zavala et al. 2019, though see references citing other trends below). One of the overdensities where this trend is observed (Wang et al. 2016, 2018) is situated in the Hyperion proto-supercluster at $z \sim 2.5$ (Cucciati et al. 2018), a structure that is probed as part of the sample presented here (though see Champagne et al. 2021 for a different view). Recent observations of the most massive proto-cluster in Hyperion, Theia, using the NOrthern Extended Millimeter Array (NOEMA) also suggest a deficit of gas among the massive galaxies of that system, which implies this trend persists to some level throughout Hyperion (Cucciati et al., in prep.). Such a deficit is also seen at lower redshifts ($z \sim 0.7$; Betti et al. 2019) for galaxies in the highest-density regions of massive group/cluster environments. If such a paucity is pervasive for galaxies in proto-cluster environments at $z \sim 2$–2.5, it would help to explain the change in behavior of the SFR$-\delta_{\rm gal}$ seen between our higher- and lower-redshift samples. However, such observations remain very sparse even at these redshifts, and the opposite trend (e.g., Gómez-Guijarro et al. 2019; Tadaki et al. 2019; Aoyama et al. 2022) or a flat trend (e.g., Lee et al. 2017; Darvish et al. 2018) of $\mu_{\rm gas}$ with environment is also observed at these redshifts (also see the discussion in §3.4 of Tacconi et al. 2020). While it appears likely that in situ gas depletion at $z \lesssim 2.5$ and gas enhancement at $z \gtrsim 2.5$ in high-density environments helps to drive the behavior of the SFR$-\delta_{\rm gal}$ relation seen here, future work with ALPINE and other observations from ALMA and PdBI at these redshifts are required in order to be able to make definitive claims.

3.5.2. Merging activity and the SFR$-\delta_{\rm gal}$ relation

It has already been established that at least some of the galaxies in the high-redshift range of the VUDS+ sample are undergoing major merging events. This evidence comes from detailed observations of individual merging systems (Jones et al. 2020; Ginolfi et al. 2020a) and from a general analysis of the PCl J1001+0220 proto-cluster, in which the VUDS members are seen to potentially show elevated numbers of companions (Lemaux et al. 2018). Additionally, there is evidence, at least up to $z \sim 2$–4, that the major merger rate broadly increases with

increasing redshift (e.g., López-Sanjuan et al. 2013; Tasca et al. 2014). Further, it has been shown that a large number of merging events in intermediate density environments, such as those in proto-clusters, are required at high redshift to explain the stellar mass function in group and cluster galaxies at $z \sim 1$ (Tomczak et al. 2017). Given this evidence, it is possible merging activity is generally prevalent in our sample, though to a lesser extent in the lower-redshift portion of our sample ($z \sim 2.5$).

The drop in merging activity from higher to lower redshift observed in the field would likely be exacerbated in higher-density environments due to dynamical considerations. Specifically, for a given structure, the velocity dispersion of member galaxies will increase with decreasing redshift as a result of the concentration of mass in the forming cluster (see, e.g., Fig. 4 of Cucciati et al. 2014), which will ultimately discourage merging activity in the cores of such structures at lower redshifts. If such merging activity serves to enhance star formation (e.g., Hopkins et al. 2008), it is possible that changes in the merging rate could explain the increase in SFR seen in higher-density environments at higher redshift and the subsequent decline to lower redshifts as such activity begins to wane.

Considering the high-M_* galaxies only, galaxies which are more likely to be strongly clustered at these redshifts than their lower-mass counterparts (see, e.g., Durkalec et al. 2018), the median overdensity in the Peak region in the highest-redshift bin for such galaxies is $\sim$5 gal Mpc^2. This translates to an average inter-galaxy distance of $\sim$0.45 Mpc. For illustrative purposes, an average velocity offset $\Delta_v = 400\,\mathrm{km\,s^{-1}}$ can be assumed for such galaxies, as this is a typical line-of-sight member velocity dispersion for member galaxies of massive proto-clusters at these redshifts (e.g., Cucciati et al. 2014, 2018; Dey et al. 2016; Toshikawa et al. 2020). Incorporating the median stellar mass of the high-M_* sample at these redshifts, $\log(\tilde{M}_*/M_\odot) = 10.30$, the resultant average dynamical friction timescale is $\sim$500 Myr (Binney & Tremaine 1987; Burke & Collins 2013). The difference in lookback times between the median redshift of galaxies in the two redshift bins used in this paper ($z = 2.34$ to $z = 3.13$) is $\sim$800 Myr in our adopted cosmology. This amount of time allows for galaxies that begin merging in the higher-redshift bin to coalesce, with several 100 megayears after coalescence to begin the transition to lower levels of SFR.

Following this line of thought, we consider two toy scenarios. In the first we assume galaxies in the higher-mass bin have a constant SFR of $\log(\mathrm{SFR}/M_\odot/\mathrm{yr}) = 1.8$, a value intermediate to the average SFR of high-M_* galaxies in the lower- and higher-redshift samples, and that such activity persists over the time period elapsed between the two redshift bins. Adding the resultant newly created stellar mass to the average stellar mass of the high-M_* galaxies in the higher-z bin, the average merger remnant formed through merging processes that began in the higher-redshift bin approaches $\log(M_*/M_\odot) = 11$ by the redshift range of our lower-redshift bin. This stellar mass rivals some of the most massive galaxies observed at these redshifts (e.g., Tomczak et al. 2014; Forrest et al. 2020; Shen et al. 2021) and begins to approach the stellar mass of the most massive cluster galaxies observed at intermediate and low redshift (see Ascaso et al. 2014 and references therein). Many such galaxies are still observed to be star forming at $z = 1$–2, though typically at modest levels, making this a plausible scenario for the formation of such galaxies.

If, conversely, merging galaxies in the highest-redshift bin have already coalesced and are experiencing relatively short-lived elevated star-formation activity as a result of this coalescence, they would have $\sim$800 Myr to begin to transition to a more quiescent state as the result of secular or larger scale environmental processes. Such a timescale is sufficient to begin to transition to quiescence for those galaxies whose SFHs are governed by an exponential decline with a relatively small τ value (e.g., Moutard et al. 2016). However, the lack of an anticorrelated SFR$-\delta_{\mathrm{gal}}$ trend for high-M_* galaxies in the lower-redshift end of the VUDS+ sample precludes this τ from being too small unless they quench so rapidly as to be outside the star-forming selection criteria of the VUDS+ spectral sample. In this case, such a small τ would require a large number of truly quiescent galaxies to be formed in such environments.

These two scenarios should lead to significantly different behavior in the stellar mass function for quiescent and star-forming galaxies as a function of both redshift and environment. Future observations from NIR spectrographs in these environments aimed at constraining the pervasiveness of high-M_* quiescent galaxies will, when paired with data sets such as the one presented here, allow for robust constraints on the timescale and manner of quenching (as done in, e.g., Balogh et al. 2016; Foltz et al. 2018; Lemaux et al. 2019; Tomczak et al. 2019 at intermediate redshifts) and the amount of merging activity in different environments (as done in, e.g., Tomczak et al. 2017). Additional future work on constraining the recent SFHs of galaxies (e.g., Cassarà et al. 2016; Carnall et al. 2019; Leja et al. 2019) in higher-density environments, especially those at high M_*, would be extremely useful to evaluate the likelihood of such scenarios.

We note, though, that the value quoted for the dynamical friction timescale, a value upon which these scenarios are predicated, should be considered a soft lower limit to the true average dynamical friction timescale as this estimate ought to be based on the true volume density of such galaxies rather than the surface density. We do not attempt a conversion here, as the true three dimensional structure of overdense regions is masked by peculiar motions. However, if the mean separation between galaxies in the Peak region is, in reality, even only $\sim$50% larger, there is little chance that galaxies, which have just begun to merge in the highest-redshift bin, have completed this process by the lower-redshift bin. In such a case, while star-formation activity could naturally be enhanced by merging processes in the higher-redshift bin, there is no natural explanation as to why such activity would begin to depreciate in our lower-redshift bin unless larger-scale processes begin to act while merging is still ongoing. Future work characterizing the frequency of merging signatures in the VUDS+ sample across different environments at fixed M_* for those galaxies imaged with the requisite resolution and depth to detect such signatures will be crucial to assess the veracity of such scenarios.

3.5.3. Large scale processes and the SFR$-\delta_{\mathrm{gal}}$ relation

It is a distinct possibility, however, that larger-scale processes may be preferentially acting on galaxies in the lower-redshift portion of our sample. Observational evidence exists for at least one overdensity at $z \sim 2.5$ to contain a hot intracluster medium (ICM), an overdensity that is in our sample (Wang et al. 2016; though again see Champagne et al. 2021 for a different possibility). Indeed, as mentioned earlier, in this particular overdensity, massive galaxies toward the center of the structure possibly appear to be deficient in their gas content relative to galaxies near the outskirts, a deficiency that may be due to stripping processes associated with the dense environment (Wang et al. 2018). Additionally, it appears that it might be a general characteristic,

at least of massive proto-clusters to begin to transition from a relatively cold ICM marked by strong absorption of neutral hydrogen (e.g., Lee et al. 2016; Newman et al. 2020) to a gravitationally heated ICM at redshifts that mark the boundary between our two redshift bins (Overzier 2016). Other case studies that probe representative galaxy populations at similar redshifts also show hints that star-formation activity in the densest regions is beginning to slow, potentially due to the presence of a hot ICM (e.g., Shimakawa et al. 2018b). Thus, it is natural to suspect that the development and heating of this ICM may be at least partially responsible for the observed reduction in the average SFR of galaxies in the Peak regions from $z \sim 3.1$ to $z \sim 2.3$, and that such a drop could occur without the need to invoke a widespread merging scenario.

The dynamical timescale for galaxies in the highest-redshift bin that are accreting into proto-cluster environments, a quantity that is defined as the time from infall at $R_{\rm vir}$ to first pericentric passage, is ∼0.3 Gyr adopting the formalism of Wetzel (2011) and Wetzel et al. (2013). Such a timescale implies that a galaxy situated deep in the core region[20] is able to make at least one or two passages through the proto-cluster core in the time elapsed between the two redshift bins in our sample. Such passages may have several consequences including decreasing the merging time of any ongoing mergers through tidal torquing, tidal stripping of the in situ or circumgalactic H I gas, and, if a hot ICM begins to develop, ram pressure stripping (see, e.g., Cen et al. 2014; Boselli et al. 2016; Steinhauser et al. 2016; Gavazzi et al. 2018; Moretti et al. 2018). Stellar feedback induced through merging activity or through elevated levels of star formation, as well as any associated active galactic nuclei (AGN) activity (see, e.g., Shimakawa et al. 2018a), would likely only serve to increase the effectiveness of such stripping (Bahé & McCarthy 2015; Lemaux et al. 2017) as otherwise usable gas is pushed to larger galactocentric radii to eventually enhance and enrich the ICM. Such feedback processes are likely more common and more severe in our higher-M_* galaxies. This sub-sample contains the galaxies that are observed with the highest average SFRs of all galaxies in VUDS+. Such elevated SFRs serve to increase the potency of stellar feedback processes (e.g., Heckman et al. 2015; Cicone et al. 2016; Ginolfi et al. 2020b) and, though perhaps not causally, increase likelihood of various types of AGN activity (Juneau et al. 2013; Lemaux et al. 2014b; Aird et al. 2019). It is indeed these galaxies that are inferred to be preferentially quenching from the higher- to the lower-redshift bin in our own data.

While such a scenario appears to satisfy at least some trends observed here and in the literature, considerable effort will need to be made to test scenarios such as these through the use of simulations and models that encode merging activity and the enrichment of the ICM. Additionally, future work will be done as part of the C3VO survey to characterize the entire population of VUDS proto-clusters and groups in the same manner as was done at $z \sim 1$ in Hung et al. (2020, 2021). In concert with the exquisite X-ray and other ancillary data available in the VUDS fields, the large number of overdensities that will be identified through our galaxy density mapping and overdensity detection approach will enable a comprehensive search for evidence of a hot ICM both in individual cases and through stacked analysis. Such a search will ultimately allow us to tie the presence or absence of a hot ICM in different structures to the properties of the galaxies contained within those structures. Through the use of simulations and semiempirical models, such evolution can eventually be connected to galaxy populations at low to intermediate redshifts ($0 \leq z \lesssim 1.5$) where a clear anticorrelation between star-formation activity and environment is observed.

[20] We note that $R_{\rm vir}$ or its counterpart R_{200} is very small at these redshifts, with $R_{200} \sim 225$ kpc at $z = 3.13$ for a proto-cluster with $M_{200} = 5 \times 10^{13}\,M_\odot$.

4. Summary and conclusions

In this paper we use a sample of 6730 star-forming galaxies spectroscopically confirmed at $2 \leq z_{\rm spec} \leq 5$ in three extragalactic legacy fields (COSMOS, ECDFS, and CFHTLS-D1) to investigate the relationship between the average SFR of galaxies, as measured by spectral energy distribution fitting, and their local environment ($\delta_{\rm gal}$). These spectroscopic data were drawn primarily from the VIMOS Ultra Deep Survey and supplemented by a variety of other spectral surveys taken across the three fields, including new observations taken with Keck/DEIMOS as part of the C3VO survey. These data were supplemented by high-quality photometric redshift measurements, which were used in conjunction with the spectroscopic data to estimate the galaxy density field at these redshifts through a technique known as Voronoi Monte Carlo mapping. While at low to intermediate redshift ($z \lesssim 1.5$) it has been shown that SFR and $\delta_{\rm gal}$ are generally anticorrelated, at $2 \leq z \leq 5$ we observe a reversal of the SFR$-\delta_{\rm gal}$ relation, with the two quantities showing a weak but significant positive correlation over more than an order of magnitude in local density. We list our main conclusions below:

- The full spectral sample, which probes from rarefied field environments to the core of massive proto-clusters, exhibits a nearly monotonic rise in SFR over more than an order of magnitude in local overdensity. Similar behavior is observed between stellar mass (M_*) and local overdensity.
- The reversal of the SFR$-\delta_{\rm gal}$ relation is observed across all three fields and across all redshifts probed by our sample with varying degrees of strength and significance. The reversal remains significant after taking into account all measurement uncertainties and selection effects, including the possible contribution of extremely dusty star-forming and quiescent galaxies that are largely absent from our sample.
- A positive SFR$-\delta_{\rm gal}$ relation is also observed at fixed M_*, with the strongest and most significant positive correlation seen among the most massive galaxies in our sample ($\log(M_*/M_\odot) \geq 10$). After accounting for and removing both redshift and stellar mass effects from the SFR$-\delta_{\rm gal}$ relation, a weaker, but still highly significant positive correlation is observed.
- The SFR$-\delta_{\rm gal}$ relation in the higher-redshift portion of the sample ($2.7 < z \leq 5$) is observed to be considerably stronger than in the lower-redshift portion of our sample ($2 \leq z \leq 2.7$). For environments that correspond to the outskirts and core of proto-clusters, termed "Intermediate" and "Peak" regions, no significant correlation is observed between SFR$-\delta_{\rm gal}$ at $2 \leq z \leq 2.7$, with galaxies in the field and the densest proto-cluster environments showing statistically consistent SFRs. Conversely, in the higher-redshift portion of our sample, a highly significant positive SFR$-\delta_{\rm gal}$ relation is found, with galaxies in the densest proto-cluster environments exhibiting average SFRs >0.5 dex higher than those in the coeval field.
- The observed SFR$-\delta_{\rm gal}$ is generally consistent with investigations in other works of this relation in the Millennium, IllustrisTNG, and other simulations, with the magnitude of the increase in the average SFR observed to be broadly

similar across the full density range probed in simulations with a few exceptions.
– We explore various scenarios that could cause the increased SFR activity seen in the high-density environments at the highest redshifts probed in our sample and the subsequent decrease of this activity in such environments to $z \sim 2$. We conclude that accelerated gas depletion, merging activity, and processes related to the large-scale environment, which include those originating from the development of a hot ICM, are all plausible mechanisms to explain the observed behavior.

This work marks an important step forward in establishing the general relationship between galaxies and their environment at high redshift. However, considerable work, both with the VUDS+ sample and with larger samples in the future from Subaru/PFS and VLT/MOONS, will be necessary to begin to quantify the average contribution of the various processes in shaping the SFR$-\delta_{\rm gal}$ at high redshift. Additional work will also be needed to identify systems in such surveys that are in special stages of formation at these epochs, such as those with fractionally large populations of strongly starbursting galaxies or massive quiescent galaxies, systems that are generally more difficult or impossible to detect from an observed-frame optical/NIR perspective. Ongoing, dedicated follow up at optical, near-infrared, and sub-millimeter wavelengths of several exceptional structures in the VUDS+ sample, as well as systems that appear to be in a more typical stag of evolution, will be eventually used to understand the various pathways through which various processes might incite and suppress star-formation activity in high-density environments in the early universe.

Acknowledgements. This paper is dedicated to Dr. Olivier Le Fèvre. Though he was unable to witness its completion, it was his vision and tenacity that made this work, among countless others, possible. Based on data obtained with the European Southern Observatory Very Large Telescope, Paranal, Chile, under Large Programs 175.A-0839, 177.A-0837, and 185.A-0791. Some of the material presented in this paper is based upon work supported by the National Science Foundation under Grant No. 1908422. This work was additionally supported by the France-Berkeley Fund, a joint venture between UC Berkeley, UC Davis, and le Centre National de la Recherche Scientifique de France promoting lasting institutional and intellectual cooperation between France and the United States. This work was supported by funding from the European Research Council Advanced Grant ERC-2010-AdG-268107-EARLY and by INAF Grants PRIN 2010, PRIN 2012 and PICS 2013. RA acknowledges support from FONDECYT Regular Grant 1202007. BCL thanks Maruša Bradač for providing the time and space necessary to finish this work. BCL additionally thanks Helmut Dannerbaur and Gaël Noirot for useful discussions and the organizers of the Protoclusters: Galaxy Evolution in Confinement workshop, a workshop which stimulated discussions on this topic that improved the manuscript. We also thank the anonymous referee for the careful reading of the manuscript. This work is partially based on observations obtained with MegaPrime/MegaCam, a joint project of CFHT and CEA/IRFU, at the Canada-France-Hawaii Telescope (CFHT) which is operated by the National Research Council (NRC) of Canada, the Institut National des Science de l'Univers of the Centre National de la Recherche Scientifique (CNRS) of France, and the University of Hawaii. This work is based in part on data products produced at Terapix available at the Canadian Astronomy Data Centre as part of the Canada-France-Hawaii Telescope Legacy Survey, a collaborative project of NRC and CNRS. This work is based, in part, on observations made with the *Spitzer* Space Telescope, which is operated by the Jet Propulsion Laboratory, California Institute of Technology under a contract with NASA. We thank ESO staff for their support for the VUDS survey, particularly the Paranal staff conducting the observations and Marina Rejkuba and the ESO user support group in Garching. Some of the spectrographic data presented herein were obtained at the W.M. Keck Observatory, which is operated as a scientific partnership among the California Institute of Technology, the University of California, and the National Aeronautics and Space Administration. The Observatory was made possible by the generous financial support of the W.M. Keck Foundation. We thank the indigenous Hawaiian community for allowing us to be guests on their sacred mountain, a privilege, without which, this work would not have been possible. We are most fortunate to be able to conduct observations from this site.

References

Aird, J., Coil, A. L., & Georgakakis, A. 2019, MNRAS, 484, 4360
Aoyama, K., Kodama, T., Suzuki, T. L., et al. 2022, ApJ, 924, 74
Araya-Araya, P., Vicentin, M. C., Sodré, L., Jr, Overzier, R. A., & Cuevas, H. 2021, MNRAS, 504, 5054
Arnouts, S., Cristiani, S., Moscardini, L., et al. 1999, MNRAS, 310, 540
Arnouts, S., Le Floc'h, E., Chevallard, J., et al. 2013, A&A, 558, A67
Ascaso, B., Lemaux, B. C., Lubin, L. M., et al. 2014, MNRAS, 442, 589
Bahé, Y. M., & McCarthy, I. G. 2015, MNRAS, 447, 969
Balestra, I., Mainieri, V., Popesso, P., et al. 2010, A&A, 512, A12
Balogh, M. L., McGee, S. L., Mok, A., et al. 2016, MNRAS, 456, 4364
Balogh, M. L., Gilbank, D. G., Muzzin, A., et al. 2017, MNRAS, 470, 4168
Balogh, M. L., van der Burg, R. F. J., Muzzin, A., et al. 2021, MNRAS, 500, 358
Béthermin, M., Fudamoto, Y., Ginolfi, M., et al. 2020, A&A, 643, A2
Betti, S. K., Pope, A., Scoville, N., et al. 2019, ApJ, 874, 53
Bielby, R., Hudelot, P., McCracken, H. J., et al. 2012, A&A, 545, A23
Binney, J., & Tremaine, S. 1987, Galactic Dynamics (Princeton: Princeton University Press)
Boquien, M., Burgarella, D., Roehlly, Y., et al. 2019, A&A, 622, A103
Bose, S., Eisenstein, D. J., Hernquist, L., et al. 2019, MNRAS, 490, 5693
Boselli, A., Roehlly, Y., Fossati, M., et al. 2016, A&A, 596, A11
Boulade, O., Charlot, X., Abbon, P., et al. 2003, in Instrument Design and Performance for Optical/Infrared Ground-based Telescopes, eds. M. Iye, & A. F. M. Moorwood, Proc. SPIE, 4841, 72
Bruzual, G., & Charlot, S. 2003, MNRAS, 344, 1000
Burgarella, D., Buat, V., & Iglesias-Páramo, J. 2005, MNRAS, 360, 1413
Burke, C., & Collins, C. A. 2013, MNRAS, 434, 2856
Calzetti, D., Armus, L., Bohlin, R. C., et al. 2000, ApJ, 533, 682
Capak, P., Aussel, H., Ajiki, M., et al. 2007, ApJS, 172, 99
Cardamone, C. N., van Dokkum, P. G., Urry, C. M., et al. 2010, ApJS, 189, 270
Carnall, A. C., Leja, J., Johnson, B. D., et al. 2019, ApJ, 873, 44
Casey, C. M., Narayanan, D., & Cooray, A. 2014, Phys. Rep., 541, 45
Casey, C. M., Cooray, A., Capak, P., et al. 2015, ApJ, 808, L33
Cassarà, L. P., Maccagni, D., Garilli, B., et al. 2016, A&A, 593, A9
Cassata, P., Giavalisco, M., Williams, C. C., et al. 2013, ApJ, 775, 106
Cassata, P., Tasca, L. A. M., Le Fèvre, O., et al. 2015, A&A, 573, A24
Cen, R., Roxana Pop, A., & Bahcall, N. A. 2014, Proc. Natl. Acad. Sci., 111, 7914
Chabrier, G. 2003, PASP, 115, 763
Champagne, J. B., Casey, C. M., Zavala, J. A., et al. 2021, ApJ, 913, 110
Chartab, N., Mobasher, B., Darvish, B., et al. 2020, ApJ, 890, 7
Cheng, T., Clements, D. L., Greenslade, J., et al. 2019, MNRAS, 490, 3840
Cheng, T., Clements, D. L., Greenslade, J., et al. 2020, MNRAS, 494, 5985
Chiang, Y.-K., Overzier, R., & Gebhardt, K. 2014, ApJ, 782, L3
Chiang, Y.-K., Overzier, R. A., Gebhardt, K., et al. 2015, ApJ, 808, 37
Chiang, Y.-K., Overzier, R. A., Gebhardt, K., & Henriques, B. 2017, ApJ, 844, L23
Cicone, C., Maiolino, R., & Marconi, A. 2016, A&A, 588, A41
Cirasuolo, M., Afonso, J., Carollo, M., et al. 2014, in Ground-based and Airborne Instrumentation for Astronomy V, SPIE Conf. Ser., 9147, 91470N
Coogan, R. T., Daddi, E., Sargent, M. T., et al. 2018, MNRAS, 479, 703
Cooper, M. C., Newman, J. A., Coil, A. L., et al. 2007, MNRAS, 376, 1445
Cooper, M. C., Newman, J. A., Weiner, B. J., et al. 2008, MNRAS, 383, 1058
Cooper, M. C., Coil, A. L., Gerke, B. F., et al. 2010, MNRAS, 409, 337
Cooper, M. C., Yan, R., Dickinson, M., et al. 2012, MNRAS, 425, 2116
Croton, D. J., Springel, V., White, S. D. M., et al. 2006, MNRAS, 365, 11
Cucciati, O., Iovino, A., Marinoni, C., et al. 2006, A&A, 458, 39
Cucciati, O., Zamorani, G., Lemaux, B. C., et al. 2014, A&A, 570, A16
Cucciati, O., Davidzon, I., Bolzonella, M., et al. 2017, A&A, 602, A15
Cucciati, O., Lemaux, B. C., Zamorani, G., et al. 2018, A&A, 619, A49
Damen, M., Labbé, I., van Dokkum, P. G., et al. 2011, ApJ, 727, 1
Darvish, B., Mobasher, B., Sobral, D., Scoville, N., & Aragon-Calvo, M. 2015, ApJ, 805, 121
Darvish, B., Scoville, N. Z., Martin, C., et al. 2018, ApJ, 860, 111
Davis, M., Faber, S. M., Newman, J., et al. 2003, in Discoveries and Research Prospects from 6- to 10-Meter-Class Telescopes II, ed. P. Guhathakurta, Proc. SPIE, 4834, 161
De Lucia, G., Kauffmann, G., & White, S. D. M. 2004, MNRAS, 349, 1101
Dekel, A., Birnboim, Y., Engel, G., et al. 2009a, Nature, 457, 451
Dekel, A., Sari, R., & Ceverino, D. 2009b, ApJ, 703, 785
Dey, A., Lee, K.-S., Reddy, N., et al. 2016, ApJ, 823, 11
Diener, C., Lilly, S. J., Knobel, C., et al. 2013, ApJ, 765, 109
Diener, C., Lilly, S. J., Ledoux, C., et al. 2015, ApJ, 802, 31
Durkalec, A., Le Fèvre, O., Pollo, A., et al. 2018, A&A, 612, A42
Elbaz, D., Daddi, E., Le Borgne, D., et al. 2007, A&A, 468, 33

Faber, S. M., Phillips, A. C., Kibrick, R. I., et al. 2003, in Instrument Design and Performance for Optical/Infrared Ground-based Telescopes, eds. M. Iye, & A. F. M. Moorwood, SPIE Conf. Ser., 4841, 1657
Faisst, A. L., Schaerer, D., Lemaux, B. C., et al. 2020, ApJS, 247, 61
Fazio, G. G., Hora, J. L., Allen, L. E., et al. 2004, ApJS, 154, 10
Foltz, R., Wilson, G., Muzzin, A., et al. 2018, ApJ, 866, 136
Forrest, B., Marsan, Z. C., Annunziatella, M., et al. 2020, ApJ, 903, 47
Fukugita, M., Ichikawa, T., Gunn, J. E., et al. 1996, AJ, 111, 1748
Fumagalli, M., Franx, M., van Dokkum, P., et al. 2016, ApJ, 822, 1
Gardner, J. P., Mather, J. C., Clampin, M., et al. 2006, Space Sci. Rev., 123, 485
Gavazzi, G., Consolandi, G., Gutierrez, M. L., Boselli, A., & Yoshida, M. 2018, A&A, 618, A130
Gawiser, E., van Dokkum, P. G., Herrera, D., et al. 2006, ApJS, 162, 1
Genzel, R., Tacconi, L. J., Lutz, D., et al. 2015, ApJ, 800, 20
Ginolfi, M., Jones, G. C., Béthermin, M., et al. 2020a, A&A, 643, A7
Ginolfi, M., Jones, G. C., Béthermin, M., et al. 2020b, A&A, 633, A90
Gobat, R., Daddi, E., Onodera, M., et al. 2011, A&A, 526, A133
Gómez, P. L., Nichol, R. C., Miller, C. J., et al. 2003, ApJ, 584, 210
Gómez-Guijarro, C., Riechers, D. A., Pavesi, R., et al. 2019, ApJ, 872, 117
Greenslade, J., Clements, D. L., Cheng, T., et al. 2018, MNRAS, 476, 3336
Grogin, N. A., Kocevski, D. D., Faber, S. M., et al. 2011, ApJS, 197, 35
Gruppioni, C., Béthermin, M., Loiacono, F., et al. 2020, A&A, 643, A8
Guaita, L., Pompei, E., Castellano, M., et al. 2020, A&A, 640, A107
Hansen, S. M., Sheldon, E. S., Wechsler, R. H., & Koester, B. P. 2009, ApJ, 699, 1333
Hatch, N. A., Wylezalek, D., Kurk, J. D., et al. 2014, MNRAS, 445, 280
Hathi, N. P., Ferreras, I., Pasquali, A., et al. 2009, ApJ, 690, 1866
Heckman, T. M., Alexandroff, R. M., Borthakur, S., Overzier, R., & Leitherer, C. 2015, ApJ, 809, 147
Hildebrandt, H., Erben, T., Dietrich, J. P., et al. 2006, A&A, 452, 1121
Hill, R., Chapman, S., Scott, D., et al. 2020, MNRAS, 495, 3124
Hill, R., Chapman, S., Phadke, K. A., et al. 2022, MNRAS, 512, 4352
Hilton, M., Stanford, S. A., Stott, J. P., et al. 2009, ApJ, 697, 436
Hopkins, P. F., Hernquist, L., Cox, T. J., & Kereš, D. 2008, ApJS, 175, 356
Hung, D., Lemaux, B. C., Gal, R. R., et al. 2020, MNRAS, 491, 5524
Hung, D., Lemaux, B. C., Gal, R. R., et al. 2021, MNRAS, 502, 3942
Hwang, H. S., Shin, J., & Song, H. 2019, MNRAS, 489, 339
Ilbert, O., Arnouts, S., McCracken, H. J., et al. 2006, A&A, 457, 841
Ilbert, O., Capak, P., Salvato, M., et al. 2009, ApJ, 690, 1236
Ilbert, O., McCracken, H. J., Le Fèvre, O., et al. 2013, A&A, 556, A55
Ito, K., Kashikawa, N., Toshikawa, J., et al. 2020, ApJ, 899, 5
Jones, G. C., Béthermin, M., Fudamoto, Y., et al. 2020, MNRAS, 491, L18
Juneau, S., Dickinson, M., Bournaud, F., et al. 2013, ApJ, 764, 176
Kitzbichler, M. G., & White, S. D. M. 2007, MNRAS, 376, 2
Kodama, T., Tanaka, I., Kajisawa, M., et al. 2007, MNRAS, 377, 1717
Koekemoer, A. M., Faber, S. M., Ferguson, H. C., et al. 2011, ApJS, 197, 36
Kovač, K., Lilly, S. J., Knobel, C., et al. 2014, MNRAS, 438, 717
Kubo, M., Uchimoto, Y. K., Yamada, T., et al. 2013, ApJ, 778, 170
Kurk, J., Cimatti, A., Daddi, E., et al. 2013, A&A, 549, A63
Laigle, C., McCracken, H. J., Ilbert, O., et al. 2016, ApJS, 224, 24
Le Fèvre, O., Béthermin, M., Faisst, A., et al. 2020, A&A, 643, A1
Le Fèvre, O., Saisse, M., Mancini, D., et al. 2003, in Instrument Design and Performance for Optical/Infrared Ground-based Telescopes, eds. M. Iye, & A. F. M. Moorwood, Proc. SPIE, 4841, 1670
Le Fèvre, O., Vettolani, G., Garilli, B., et al. 2005, A&A, 439, 845
Le Fèvre, O., Cassata, P., Cucciati, O., et al. 2013, A&A, 559, A14
Le Fèvre, O., Tasca, L. A. M., Cassata, P., et al. 2015, A&A, 576, A79
Lee, K.-G., Hennawi, J. F., White, M., et al. 2016, ApJ, 817, 160
Lee, M. M., Tanaka, I., Kawabe, R., et al. 2017, ApJ, 842, 55
Lehmer, B. D., Brandt, W. N., Alexander, D. M., et al. 2005, ApJS, 161, 21
Leja, J., Carnall, A. C., Johnson, B. D., Conroy, C., & Speagle, J. S. 2019, ApJ, 876, 3
Lemaux, B. C., Lubin, L. M., Sawicki, M., et al. 2009, ApJ, 700, 20
Lemaux, B. C., Gal, R. R., Lubin, L. M., et al. 2012, ApJ, 745, 106
Lemaux, B. C., Cucciati, O., Tasca, L. A. M., et al. 2014a, A&A, 572, A41
Lemaux, B. C., Le Floc'h, E., Le Fèvre, O., et al. 2014b, A&A, 572, A90
Lemaux, B. C., Tomczak, A. R., Lubin, L. M., et al. 2017, MNRAS, 472, 419
Lemaux, B. C., Le Fèvre, O., Cucciati, O., et al. 2018, A&A, 615, A77
Lemaux, B. C., Tomczak, A. R., Lubin, L. M., et al. 2019, MNRAS, 490, 1231
Lewis, A. J. R., Ivison, R. J., Best, P. N., et al. 2018, ApJ, 862, 96
Lilly, S. J., Le Brun, V., Maier, C., et al. 2009, ApJS, 184, 218
Lilly, S. J., Le Fèvre, O., Renzini, A., et al. 2007, ApJS, 172, 70
Loiacono, F., Decarli, R., Gruppioni, C., et al. 2021, A&A, 646, A76
Long, A. S., Cooray, A., Ma, J., et al. 2020, ApJ, 898, 133
López-Sanjuan, C., Le Fèvre, O., Tasca, L. A. M., et al. 2013, A&A, 553, A78
Lower, S., Narayanan, D., Leja, J., et al. 2020, ApJ, 904, 33
Lubin, L. M., Gal, R. R., Lemaux, B. C., Kocevski, D. D., & Squires, G. K. 2009, AJ, 137, 4867
Macklin, J. T. 1982, MNRAS, 199, 1119
Madau, P., & Dickinson, M. 2014, ARA&A, 52, 415
Maraston, C., Pforr, J., Renzini, A., et al. 2010, MNRAS, 407, 830
Martin, D. C., Fanson, J., Schiminovich, D., et al. 2005, ApJ, 619, L1
Mauduit, J.-C., Lacy, M., Farrah, D., et al. 2012, PASP, 124, 714
Mawatari, K., Yamada, T., Fazio, G. G., Huang, J.-S., & Ashby, M. L. N. 2016, PASJ, 68, 46
McCracken, H. J., Milvang-Jensen, B., Dunlop, J., et al. 2012, A&A, 544, A156
McLean, I. S., Steidel, C. C., Epps, H. W., et al. 2012, in Ground-based and Airborne Instrumentation for Astronomy IV Proc. SPIE,, 8446, 84460J
Miller, T. B., Hayward, C. C., Chapman, S. C., & Behroozi, P. S. 2015, MNRAS, 452, 878
Miller, T. B., Chapman, S. C., Aravena, M., et al. 2018, Nature, 556, 469
Miyazaki, S., Komiyama, Y., Sekiguchi, M., et al. 2002, PASJ, 54, 833
Miyazaki, S., Komiyama, Y., Nakaya, H., et al. 2012, in Ground-based and Airborne Instrumentation for Astronomy IV, Proc. SPIE, 8446, 84460Z
Moretti, A., Poggianti, B. M., Gullieuszik, M., et al. 2018, MNRAS, 475, 4055
Morris, A. M., Kocevski, D. D., Trump, J. R., et al. 2015, AJ, 149, 178
Mostek, N., Coil, A. L., Moustakas, J., Salim, S., & Weiner, B. J. 2012, ApJ, 746, 124
Moutard, T., Arnouts, S., Ilbert, O., et al. 2016, A&A, 590, A103
Moy, E., Barmby, P., Rigopoulou, D., et al. 2003, A&A, 403, 493
Muldrew, S. I., Hatch, N. A., & Cooke, E. A. 2018, MNRAS, 473, 2335
Muzzin, A., Wilson, G., Yee, H. K. C., et al. 2012, ApJ, 746, 188
Muzzin, A., Marchesini, D., Stefanon, M., et al. 2013, ApJ, 777, 18
Nantais, J. B., van der Burg, R. F. J., Lidman, C., et al. 2016, A&A, 592, A161
Nantais, J. B., Muzzin, A., van der Burg, R. F. J., et al. 2017, MNRAS, 465, L104
Nelson, D., Springel, V., Pillepich, A., et al. 2019, Comput. Astrophys. Cosmol., 6, 2
Newman, J. A., Cooper, M. C., Davis, M., et al. 2013, ApJS, 208, 5
Newman, A. B., Ellis, R. S., Andreon, S., et al. 2014, ApJ, 788, 51
Newman, A. B., Rudie, G. C., Blanc, G. A., et al. 2020, ApJ, 891, 147
Noirot, G., Stern, D., Mei, S., et al. 2018, ApJ, 859, 38
Noll, S., Burgarella, D., Giovannoli, E., et al. 2009, A&A, 507, 1793
Oke, J. B., & Gunn, J. E. 1983, ApJ, 266, 713
Old, L. J., Balogh, M. L., van der Burg, R. F. J., et al. 2020, MNRAS, 493, 5987
Oteo, I., Ivison, R. J., Dunne, L., et al. 2018, ApJ, 856, 72
Overzier, R. A. 2016, A&ARv, 24, 14
Owers, M. S., Hudson, M. J., Oman, K. A., et al. 2019, ApJ, 873, 52
Paccagnella, A., Vulcani, B., Poggianti, B. M., et al. 2019, MNRAS, 482, 881
Peng, Y.-J., Lilly, S. J., Kovač, K., et al. 2010, ApJ, 721, 193
Prévot, M. L., Lequeux, J., Prevot, L., Maurice, E., & Rocca-Volmerange, B. 1984, A&A, 132, 389
Puget, P., Stadler, E., Doyon, R., et al. 2004, in Ground-based Instrumentation for Astronomy eds. A. F. M. Moorwood, & M. Iye, Proc. SPIE, 5492, 978
Quadri, R. F., Williams, R. J., Franx, M., & Hildebrandt, H. 2012, ApJ, 744, 88
Raichoor, A., Mei, S., Nakata, F., et al. 2011, ApJ, 732, 12
Rettura, A., Rosati, P., Nonino, M., et al. 2010, ApJ, 709, 512
Rodighiero, G., Renzini, A., Daddi, E., et al. 2014, MNRAS, 443, 19
Romano, M., Cassata, P., Morselli, L., et al. 2020, MNRAS, 496, 875
Ryan, R. E., Jr, Gonzalez, A. H., Lemaux, B. C., et al. 2014, ApJ, 786, L4
Santos, J. S., Altieri, B., Tanaka, M., et al. 2014, MNRAS, 438, 2565
Santos, J. S., Altieri, B., Valtchanov, I., et al. 2015, MNRAS, 447, L65
Schaerer, D., de Barros, S., & Sklias, P. 2013, A&A, 549, A4
Schaerer, D., Ginolfi, M., Béthermin, M., et al. 2020, A&A, 643, A3
Schinnerer, E., Groves, B., Sargent, M. T., et al. 2016, ApJ, 833, 112
Scoville, N., Aussel, H., Brusa, M., et al. 2007, ApJS, 172, 1
Scoville, N., Arnouts, S., Aussel, H., et al. 2013, ApJS, 206, 3
Scoville, N., Sheth, K., Aussel, H., et al. 2016, ApJ, 820, 83
Scoville, N., Lee, N., Vanden Bout, P., et al. 2017, ApJ, 837, 150
Shen, L., Lemaux, B. C., Lubin, L. M., et al. 2021, ApJ, 912, 60
Shi, K., Lee, K.-S., Dey, A., et al. 2019, ApJ, 871, 83
Shi, K., Toshikawa, J., Cai, Z., Lee, K.-S., & Fang, T. 2020, ApJ, 899, 79
Shi, K., Toshikawa, J., Lee, K.-S., et al. 2021, ApJ, 911, 46
Shimakawa, R., Kodama, T., Hayashi, M., et al. 2017, MNRAS, 468, L21
Shimakawa, R., Kodama, T., Hayashi, M., et al. 2018a, MNRAS, 473, 1977
Shimakawa, R., Koyama, Y., Röttgering, H. J. A., et al. 2018b, MNRAS, 481, 5630
Shivaei, I., Kriek, M., Reddy, N. A., et al. 2016, ApJ, 820, L23
Silverman, J. D., Rujopakarn, W., Daddi, E., et al. 2018, ApJ, 867, 92
Smolčić, V., Miettinen, O., Tomičić, N., et al. 2017a, A&A, 597, A4
Smolčić, V., Novak, M., Bondi, M., et al. 2017b, A&A, 602, A1
Socolovsky, M., Almaini, O., Hatch, N. A., et al. 2018, MNRAS, 476, 1242
Springel, V., White, S. D. M., Jenkins, A., et al. 2005, Nature, 435, 629
Steinhauser, D., Schindler, S., & Springel, V. 2016, A&A, 591, A51
Strait, V., Bradač, M., Coe, D., et al. 2021, ApJ, 910, 135
Straughn, A. N., Pirzkal, N., Meurer, G. R., et al. 2009, AJ, 138, 1022
Strazzullo, V., Gobat, R., Daddi, E., et al. 2013, ApJ, 772, 118

Strazzullo, V., Coogan, R. T., Daddi, E., et al. 2018, ApJ, 862, 64
Sugai, H., Karoji, H., Takato, N., et al. 2012, in Ground-based and Airborne Instrumentation for Astronomy IV, SPIE Conf. Ser., 8446, 84460Y
Tacconi, L. J., Genzel, R., Saintonge, A., et al. 2018, ApJ, 853, 179
Tacconi, L. J., Genzel, R., & Sternberg, A. 2020, ARA&A, 58, 157
Tadaki, K.-I., Kodama, T., Hayashi, M., et al. 2019, PASJ, 71, 40
Talia, M., Cimatti, A., Pozzetti, L., et al. 2015, A&A, 582, A80
Tasca, L. A. M., Le Fèvre, O., López-Sanjuan, C., et al. 2014, A&A, 565, A10
Tasca, L. A. M., Le Fèvre, O., Hathi, N. P., et al. 2015, A&A, 581, A54
Tasca, L. A. M., Le Fèvre, O., Ribeiro, B., et al. 2017, A&A, 600, A110
Tomczak, A. R., Quadri, R. F., Tran, K.-V. H., et al. 2014, ApJ, 783, 85
Tomczak, A. R., Quadri, R. F., Tran, K.-V. H., et al. 2016, ApJ, 817, 118
Tomczak, A. R., Lemaux, B. C., Lubin, L. M., et al. 2017, MNRAS, 472, 3512
Tomczak, A. R., Lemaux, B. C., Lubin, L. M., et al. 2019, MNRAS, 484, 4695
Tonnesen, S., & Cen, R. 2014, ApJ, 788, 133
Toshikawa, J., Kashikawa, N., Overzier, R., et al. 2014, ApJ, 792, 15
Toshikawa, J., Kashikawa, N., Overzier, R., et al. 2016, ApJ, 826, 114
Toshikawa, J., Uchiyama, H., Kashikawa, N., et al. 2018, PASJ, 70, S12
Toshikawa, J., Malkan, M. A., Kashikawa, N., et al. 2020, ApJ, 888, 89
Tran, K.-V. H., Franx, M., Illingworth, G., Kelson, D. D., & van Dokkum, P. 2003, ApJ, 599, 865
Tran, K.-V. H., Papovich, C., Saintonge, A., et al. 2010, ApJ, 719, L126
Trump, J. R., Konidaris, N. P., Barro, G., et al. 2013, ApJ, 763, L6
van der Burg, R. F. J., Rudnick, G., Balogh, M. L., et al. 2020, A&A, 638, A112
Vanzella, E., Cristiani, S., Dickinson, M., et al. 2008, A&A, 478, 83
Vanzella, E., Giavalisco, M., Dickinson, M., et al. 2009, ApJ, 695, 1163
von der Linden, A., Wild, V., Kauffmann, G., White, S. D. M., & Weinmann, S. 2010, MNRAS, 404, 1231
Wang, T., Elbaz, D., Daddi, E., et al. 2016, ApJ, 828, 56
Wang, T., Elbaz, D., Daddi, E., et al. 2018, ApJ, 867, L29
Wetzel, A. R. 2011, MNRAS, 412, 49
Wetzel, A. R., Tinker, J. L., Conroy, C., & van den Bosch, F. C. 2013, MNRAS, 432, 336
Wu, P.-F., Gal, R. R., Lemaux, B. C., et al. 2014, ApJ, 792, 16
Wuyts, S., Förster Schreiber, N. M., Lutz, D., et al. 2011, ApJ, 738, 106
Zavala, J. A., Casey, C. M., Scoville, N., et al. 2019, ApJ, 887, 183
Zhou, L., Elbaz, D., Franco, M., et al. 2020, A&A, 642, A155

[1] Aix-Marseille Univ, CNRS, CNES, Laboratoire d'Astrophysique de Marseille, Marseille, France
e-mail: brian.lemaux@noirlab.edu

[2] Department of Physics and Astronomy, University of California, One Shields Ave., Davis, CA 95616, USA
[3] Gemini Observatory, NSF's NOIRLab 670 N. A'ohoku Place, Hilo, HI 96720, USA
[4] INAF – Osservatorio di Astrofisica e Scienza dello Spazio di Bologna, Via Gobetti 93/3, 40129 Bologna, Italy
[5] Space Telescope Science Institute, 3700 San Martin Drive, Baltimore, MD 21218, USA
[6] UCO/Lick Observatory, Department of Astronomy & Astrophysics, UCSC, 1156 High Street, Santa Cruz, CA 95064, USA
[7] Instituto de Investigacíon Multidisciplinar en Ciencia y Tecnología, Universidad de La Serena, Raul Bitrán 1305, La Serena, Chile
[8] Departamento de Física y Astronomía, Universidad de La Serena, Av. Juan Cisternas 1200 Norte, La Serena, Chile
[9] Dipartimento di Fisica e Astronomia, Università di Padova, Vicolo dell'Osservatorio, 3, 35122 Padova, Italy
[10] INAF Osservatorio Astronomico di Padova, Vicolo dell'Osservatorio 5, 35122 Padova, Italy
[11] University of Hawai'i, Institute for Astronomy, 2680 Woodlawn Drive, Honolulu, HI 96822, USA
[12] INAF–IASF,Via Bassini 15, 20133 Milano, Italy
[13] INAF–Osservatorio Astronomico di Roma, Via di Frascati 33, 00040 Monte Porzio Catone, Italy
[14] Núcleo de Astronomía, Facultad de Ingeniería, Universidad Diego Portales, Av. Ejército 441, Santiago, Chile
[15] Astronomy Department, University of Massachusetts, Amherst, MA 01003, USA
[16] Leiden Observatory, Leiden University, PO Box 9513, 2300, RA Leiden, The Netherlands
[17] Geneva Observatory, University of Geneva, Ch. des Maillettes 51, 1290 Versoix, Switzerland
[18] CAS Key Laboratory for Research in Galaxies and Cosmology, Department of Astronomy, University of Science and Technology of China, Hefei 230026, PR China
[19] School of Astronomy and Space Sciences, University of Science and Technology of China, Hefei 230026, PR China
[20] European Southern Observatory, Av. Alonso de Córdova 3107, Vitacura, Santiago, Chile

Appendix A: Modification to the VMC method in the VUDS+ mapping

In §2.4 we described the base VMC method used for the mapping, which is identical to that adopted by earlier works that implemented VMC-based density mapping. In this Appendix, we discuss the slight modification that we made to this method for the purposes of this study. For each Monte Carlo realization of each redshift slice in the VMC map, we first selected the spectroscopic subsample by drawing from a uniform distribution ranging from 0 to 1 and retaining those $z_{\rm spec}$ measurements where the number drawn was below a certain likelihood threshold set for that slice and iteration for all galaxies flags=X2/X9 and X3/X4. As a reminder, those galaxies with flag=X1 never had their spectral information used. The likelihood threshold of each flag was determined by the reliability of a $z_{\rm spec}$ measurement with a given flag, which was estimated from ∼200 objects that were independently observed multiple times as part of the VUDS survey. From these ∼200 objects, we estimated, for each flag, from the number of observations that yielded statistically identical redshift measures both a likelihood of a redshift of a given flag to be reproducible in independent observations with independent measurements as well as its associated uncertainty. Due to small numbers, objects assigned a flag=X9 were treated in combination with those assigned a flag=X2 and objects assigned a flag=X3 were grouped with flag=X4 objects. The likelihood values and their associated uncertainties were $0.70^{+0.04}_{-0.06}$ and $0.993^{+0.004}_{-0.006}$ for flags=X2/X9 and flags=X3/X4, respectively. Though we do not use them in this study, this same exercise was performed for flag=X1 objects and returned a likelihood value of $0.41^{+0.06}_{-0.08}$, a relatively high value given this is the lowest confidence flag assigned to objects that have some detectable signal. These thresholds depart slightly from the values listed in Le Fèvre et al. 2015 due to the differing methodology used to assess the reliability of the flags. We note that the final VUDS+ spectroscopic sample contains roughly equal numbers of flag=X2/X9 and flag=X3/X4 objects (47%–53%, respectively).

To determine the threshold for flags=X2/X9 and X3/X4 objects for a given iteration and slice, a Gaussian was sampled with a mean and dispersion corresponding to the likelihood values and their associated uncertainties above. For each flag combination, this sampling would set the threshold for a given iteration/slice. For example, a sampling value of $+1\sigma$ for the flag=X2/X9 objects would set the threshold for those objects to $0.70 + 0.04 = 0.74$ in that iteration/slice. For each object, if the determined threshold for the appropriate flag value was not exceeded, $z_{\rm spec}$ would be retained for that realization, otherwise the $z_{\rm phot}$ information was instead used. For each object where the $z_{\rm phot}$ information was adopted, or was the only information available, the original $z_{\rm phot}$ for that object was perturbed by sampling from an asymmetric Gaussian distribution with σ values that correspond to the lower and upper effective 1σ $z_{\rm phot}$ uncertainties. This treatment generated a unique set of redshifts for our entire sample for each iteration of each redshift slice from which to select the objects to Voronoi tessellate over. Results of preliminary tests on the accuracy and precision of various incarnations of this method are discussed in Tomczak et al. (2017) and Lemaux et al. (2018). Additionally, the effectiveness of a version of this method to recover groups and clusters in the intermediate redshift ORELSE (Lubin et al. 2009) survey is discussed in detail in Hung et al. (2020) and will be discussed in the context of the VUDS and C3VO surveys in a future work.